Loss of full-length dystrophin expression results in major cell-autonomous abnormalities in proliferating myoblasts.

Maxime R. F. Gosselin[1], Virginie Mournetas[2], Malgorzata Borczyk[3], Suraj Verma[4], Annalisa Occhipinti[4], Justyna Róg[1,5], Lukasz Bozycki[1,5], Michal Korostynski[3], Samuel C. Robson[1,6], Claudio Angione[4], Christian Pinset[7], Dariusz C. Górecki[1] *

[1]School of Pharmacy and Biomedical Sciences, University of Portsmouth, PO1 2DT, Portsmouth, UK

[2]INSERM UEVE UMR861, I-STEM, AFM, 28 rue Henri Desbruères, 91100 Corbeil-Essonnes, France

[3]Laboratory of Pharmacogenomics, Maj Institute of Pharmacology PAS, Krakow, Poland

[4]School of Computing, Engineering and Digital Technologies, Teesside University, UK

[5]Laboratory of Cellular Metabolism, Nencki Institute of Experimental Biology, Warsaw, Poland

[6]Centre for Enzyme Innovation, University of Portsmouth, PO1 2DT, Portsmouth, UK

[7]CNRS, I-STEM, AFM, 28 rue Henri Desbruères, 91100 Corbeil-Essonnes, France

*Corresponding author (darek.gorecki@port.ac.uk)

Keywords

DMD, dystrophin, mdx, myoblast, transcriptomics

Abstract

Duchenne muscular dystrophy (DMD) affects myofibers and muscle stem cells (SC), causing progressive muscle degeneration and repair defects. It was not known whether dystrophic myoblasts—the effector cells of muscle growth and regeneration—are affected. Using a combination of transcriptomic, molecular, functional analyses, and genome-scale metabolic modelling, we demonstrate, for the first time, convergent cell-autonomous abnormalities in primary mouse and human dystrophic myoblasts. In *Dmd*^{mdx} mouse myoblasts lacking full-length dystrophin transcripts, the expression of 170 other genes was significantly altered. Myod1 (p=2.9e-21) and key muscle genes controlled by MyoD (Myog, Mymk, Mymx, epigenetic regulators, ECM interactors, calcium signalling and fibrosis genes) were significantly downregulated. Gene ontology enrichment analysis indicated significant alterations in genes involved in muscle development and function. These transcriptomic abnormalities translated into functional alterations such as increased proliferation (p=3.0e-3), reduced chemotaxis towards both sera-rich (p=3.8e-2) and cytokine-containing medium (p=1.0e-2), and significantly accelerated

differentiation in 3D organotypic cultures. These altered myoblast functions are essential for muscle regeneration. The defects were caused by the loss of expression of full-length dystrophin, as strikingly similar and not exacerbated alterations were also observed in dystrophin-null *Dmd*$^{mdx-\beta geo}$ myoblasts. Corresponding abnormalities were identified in an established dystrophic mouse muscle (SC5) cell line and human DMD primary myoblasts, confirming universal, cross-species and cell-autonomous nature of these defects. The genome-scale metabolic analysis in human DMD myoblasts indicated significant alteration in the rate of glycolysis/gluconeogenesis (log2FC = 4.8), leukotriene metabolism (log2FC = 4.754), mitochondrial beta-oxidation of branched-chain, odd-chain, and di-unsaturated fatty acids (n-6) (log2FC = -1.187 , log2FC = -0.8295 and log2FC = -0.655). These results demonstrate the disease continuum: DMD defects in satellite cells cause myoblast dysfunctions affecting muscle regeneration, which is essential to counteract myofiber loss. Contrary to the established belief, our data demonstrate that typical DMD alterations occur in myoblasts, making these cells a novel therapeutic target for the treatment of this lethal disease.

Introduction

Duchenne muscular dystrophy (DMD) is a debilitating and lethal neuromuscular disorder caused by mutations in the *DMD* gene located on the X chromosome [1]. Diagnosis is made between the age of 2 and 5, loss of ambulation occurs around 12 and young adults die due to respiratory and/or cardiac failure [2].

DMD is the largest human gene known [3]: Three full-length transcripts encode 427 kDa proteins, while further intragenic promoters drive the expression of progressively truncated variants. Dp427 and the dystrophin-associated protein complex (DAPC) are important for the functional development of differentiating myotubes [4] and subsequently prevent contraction-induced injury in the mature muscle[5].

Several studies showed that the ablation of dystrophin in fully differentiated myofibres did not trigger their degeneration [5,6], and even that myofibres can function without dystrophin [7,8].

In fact, DMD pathology is active prior to diagnosis: delays in the attainment of motor and non-motor milestones are discernible in 2 months old DMD babies [9] and transcriptomes of muscles from asymptomatic DMD patients revealed typical dystrophic abnormalities [10]. Studies of human foetuses [11–13] and various animal DMD models, including GRMD dogs [14], Sapje zebrafish [15] and *Dmd*^{mdx} mouse embryos [16] revealed that pathology starts already in prenatal development.

Indeed, in skeletal muscle lineages modelled in human DMD pluripotent stem cells, we have recently demonstrated marked transcriptome and miRNA dysregulations identifiable even before muscle specialisation [17]. These data, combined with the existence of the specific embryonic dystrophin Dp412e [18], substantiate the early disease manifestations in muscle precursor cells.

Importantly, there is increasing evidence that dysregulation of myogenic cells is behind muscle pathology and disease progression in adult DMD muscle. However, the mechanism(s) remain(s) to be elucidated and, given the interaction of myogenic and inflammatory cells in muscle regeneration [19], distinguishing the primary and the secondary consequences of dystrophin deficiency is crucial for the development of effective therapies.

Helen Blau proposed that DMD is intrinsic to the undifferentiated myoblast [20]. This hypothesis was initially discounted [21], but there is new evidence that *DMD* mutations produce a range of cell-autonomous abnormalities in both human and mouse myogenic cells from adult muscles [22–25].

If DMD directly affects myoblasts, cells that are key to muscle regeneration, a better definition of the consequences of the loss of *DMD* gene expression could help identify early disease biomarkers and establish better therapeutic targets.

Herein, using a combination of RNA-Seq, molecular and functional approaches, we compared the dystrophic and healthy myoblasts isolated from skeletal muscles of the commonly used *Dmd*$^{\mathrm{mdx}}$ mouse model. The *Dmd*$^{\mathrm{mdx}}$ has a stop codon mutation in exon 23 [26] resulting in the loss of full-length (Dp427) dystrophin expression, which reflects the molecular defect affecting the majority of DMD patients. Detailed histological and molecular analyses indicated that the clinical phenotype in 3 to 10 weeks old *Dmd*$^{\mathrm{mdx}}$ is as aggressive as in Duchenne patients [27–29]. Therefore, during this period, *Dmd*$^{\mathrm{mdx}}$ is a good model for the human pathology. Unlike human, after this phase of severe degeneration-regeneration, most *Dmd*$^{\mathrm{mdx}}$ muscles start to regenerate [28] due to an unknown mechanism.

While Dp427 is expressed in satellite cells and myofibres and its loss in *Dmd*$^{\mathrm{mdx}}$ reflects the predominant molecular defect in DMD patients, dystrophin Dp71 is present in regenerating muscles and specifically in myoblasts [30]. Yet, little attention has been given to the DMD pathology in the dystrophin-null individuals. Given that we have recently described exacerbated pathology in *Dmd*$^{\mathrm{mdx}\text{-}\beta\mathrm{geo}}$ mice lacking all dystrophins [31], we also investigated the consequences of the total loss of *Dmd* expression in *Dmd*$^{\mathrm{mdx}\text{-}\beta\mathrm{geo}}$ myoblasts [32].

Finally, we compared transcriptomic alterations in mouse and human dystrophic myoblasts to identify defects occurring across species. Given that skeletal muscle is a key metabolic site, accounting for around 90% of total oxygen uptake, muscle metabolism is a significant variable [33]. Moreover, metabolic dysfunction can impair muscle regeneration, and the impact of DMD on cellular energetics in muscle progenitors has recently been identified [34]. Therefore, using the RNA-

Seq profiles, we reconstructed the human myoblast-specific enzyme-constrained genome-scale metabolic model.

We report that the absence of expression of the full-length dystrophin triggers major transcriptomic and functional abnormalities in myoblasts. These abnormalities are cell autonomous, as they persist in myogenic cells maintained long-term in culture. Importantly, key alterations are common between mouse and human myoblasts.

Results

Transcriptomic alterations in proliferating Dmd^{mdx} myoblasts

Total RNA extracted from primary myoblasts isolated from gastrocnemii of 8-week-old male *Dmd*^{mdx}, *Dmd*$^{mdx\beta geo}$ and control mice was subjected to RNA-Seq and analysed for the differential expression of genes between groups and the enrichment of GO categories in the generated lists of differentially expressed genes.

Bioinformatic analysis of the RNA-Seq data showed the impact of the *Dmd*^{mdx} allele on the primary myoblast transcriptome. Sample-based hierarchical clustering clearly segregates genes into two groups corresponding to genotypes (Figure 1a) and a volcano plot illustrates the presence of a substantial number of significantly dysregulated genes (Figure 1b; Table S1).

The expression of 170 genes was found to be significantly up- or down-regulated more than 2-fold when comparing *Dmd*^{mdx} and WT primary mouse myoblasts (Table S1). Among these, *Myod1* and *Myog,* key coordinators of skeletal muscle development and repair, were found to be downregulated in dystrophic myoblasts and their downregulation was confirmed by qPCR (Figure S1). *Pax3* and *Pax7* transcriptional regulators [35] were also individually investigated, with Pax3 levels confirmed as significantly downregulated by qPCR (Figure S1). Our analysis identified downregulation of further important regulators and effectors of the muscle program (Figure 1c; Table S1) such as *Mymx and Bex1*, known to be regulators of muscle repair [36]. *Des*, a structural component of myofilaments, and *Itga7*, the primary laminin-1 receptor of myoblasts and mature fibres were also found to be significantly downregulated (Figure 1c; Table S1).

The *H19* gene, defined as promoting differentiation [37], was found to be significantly downregulated in proliferating *Dmd*^{mdx} myoblasts (Figure 1c; Table S1), which combined with reduced expression of aforementioned muscle program markers, as well as myogenic differentiation markers such as *Acta1*, *Actc1*, *Actn3*, *Atp2a1* and upregulation of *Nov,* known to inhibit myogenic differentiation [38], imply an altered readiness of dystrophic myoblasts to differentiate. Moreover, numerous genes encoding histones and *Smyd1* [39] and *Hmga1* [40,41] regulators of chromatin organisation/chromatin interacting proteins, were found to be significantly dysregulated in dystrophic myoblasts (Figure 1c; Table S1). Taken together, these gene expression changes indicated an increased readiness of dystrophic myoblasts to proliferate, compared to their WT counterparts.

Several genes key to myoblast-extracellular matrix interactions and fibrosis were found to be significantly dysregulated in *Dmd*$^{\mathrm{mdx}}$ myoblasts (Figure 1c; Table S1), including: *Mmp3*, *Mmp9* and *Mmp10* metalloproteases*,* collagen genes (*Col2a1*, *Col4a1*, *Col4a2* and *Col8a2*), *Lrrn1* a transmembrane protein interacting with fibronectin [42] as well as genes encoding fibronectin itself (*Fn1*) and decorin (*Dcn*). The latter promotes proliferation and differentiation in myoblasts [43] but also has a role in collagen assembly and mineralisation [44].

Finally, calsequestrins (*Casq1* and *Casq2*) (Table S1) were significantly downregulated, in line with previous observations in the dystrophic muscle [45].

No exacerbation of transcriptomic alterations in the dystrophin-null Dmd$^{\mathit{mdx}\text{-}\beta\mathit{geo}}$ *compared to Dmd*$^{\mathit{mdx}}$ *myoblasts*

Corresponding bioinformatic comparison of *Dmd*$^{\mathrm{mdx}\text{-}\beta\mathrm{geo}}$ vs. *Dmd*$^{\mathrm{mdx}}$ myoblast transcriptomes found no substantial difference between them, as illustrated by sample clustering (Figure 2a) and volcano plot (Figure 2b), with no segregation between groups. Only 11 genes were found to be significantly differentially expressed between the two genotypes. Of these, 6 are pseudogenes, 1 is a processed transcript and only 4 are protein-coding genes (*Igf1*, *Npr3*, *Postn* and *Capn6*). None of these genes has a higher log2 fold change than 1.7 and the adjusted *p*-values have an average of 1.0e-2 compared to $9.6.10^{-3}$ for the genes found to be significantly differentially expressed between *Dmd*$^{\mathrm{mdx}}$ and WT myoblasts.

Interestingly, a comparison of the *Dmd*$^{\mathrm{mdx}\text{-}\beta\mathrm{geo}}$ to the WT transcriptome returned fewer (81) (Table S2) significantly differentially expressed genes than *Dmd*$^{\mathrm{mdx}}$ versus WT (170) (Table S1). However, a comparison of the fold changes between the two analyses (Figure 2c) revealed that the two models show strikingly similar alterations with a strong, significant correlation ($r = 0.9418$, $p< 1.0e\text{-}4$) in the log2 fold changes for genes significantly altered in *Dmd*$^{\mathrm{mdx}}$ versus WT and/or *Dmd*$^{\mathrm{mdx}\text{-}\beta\mathrm{geo}}$ versus WT analyses (Figure 2c).

MyoD-dependent downregulation of gene expression in dystrophic myoblasts

Lists of genes altered in dystrophic myoblasts were analysed for common patterns of transcriptional regulation. Overrepresented transcription factor binding sites (TFBS) on promoter regions of the dysregulated genes were examined using the seqinspector tool and available ChIP-Seq data [46]. Genes found downregulated in Dmd^{mdx} had increased ChIP-Seq signal at the TFBS for four transcription factors: MyoD (adjusted *p*-value: $2.9e^{-21}$, track GEO accession GSM915165), TCF12 ($1e^{-19}$, GSM915178), MYOG ($5.6e^{-19}$, GSM915164) and TCF3 (adjusted *p*-value 3.3e-3, GSM915177) (Figure 3; Table S3B). A range of genes, including *Mymk, Mymx, Chrna1* and *Acta1* showed a binding signal at their TFBS above the background of at least three out of four of these overrepresented TFs (Figure 3b; Table S3C). Furthermore, transcripts downregulated in $Dmd^{mdx\text{-}\beta geo}$ also exhibit overrepresentation of MyoD binding sites (Table S3E). In contrast, genes upregulated in any cell type under investigation did not show any statistically significant overrepresentation of the binding signal of any TF (Table S3A and D).

GO enrichment analysis indicates significant functional alterations in dystrophic myoblasts

Two broad GO categories: “muscle system process” and “regulation of muscle system process” were enriched in the downregulated genes found when comparing Dmd^{mdx} and $Dmd^{mdx\text{-}\beta geo}$ vs. WT primary mouse myoblasts (Figure 4a; Table S4). These categories include genes involved in muscle development and function. For a myoblast to fulfil its role in regenerating a damaged muscle, it must be able to proliferate, migrate towards and differentiate in response to relevant stimuli. GO enrichment analyses of downregulated genes (Figure 4; Table S4) imply phenotypic alterations in dystrophic myoblasts affecting all three functions.

Specifically, categories such as “chromatin assembly” and “muscle cell proliferation” (Figure 4b; Table S4), are enriched, indicating an altered proliferative state of dystrophic myoblasts. The enrichment of the GO categories “muscle cell migration” and “positive regulation of cell migration” in downregulated genes (Figure 4; Table S4) indicate a migrative phenotype in dystrophic myoblasts, while GO categories “muscle cell differentiation” and “striated muscle cell differentiation” (Figure 4a and b; Table S4) suggest that dystrophic myoblasts may have an altered ability to differentiate.

Moreover, several GO categories related to calcium ion transport, homeostasis and calcium-mediated signalling were found significantly enriched in Dmd^{mdx} vs. WT downregulated genes (Figure 4b; Table S4), in line with this well-established dystrophic abnormality [47].

These results suggested alterations in proliferation, migration, and differentiation in both Dmd^{mdx} and $Dmd^{mdx\text{-}\beta geo}$ cells. To further assess these processes, we performed functional analyses of these three key myoblast functions in primary myoblasts isolated from gastrocnemii of dystrophic and control mice.

Increased proliferative capacity of dystrophic myoblasts

The ability of myoblasts to proliferate is key to obtaining enough myogenic cells to repair muscle fibre damage. Given that the transcriptomic data indicated this mechanism as likely to be affected, we tested, in a BrDU incorporation assay, the dystrophic myoblasts' capacity to respond to the proliferative stimulus of the exposure to a sera-rich medium (Figure 5a). After six hours, 57 % of *Dmd*^{mdx} myoblasts have incorporated BrDU compared to 26 % of WT cells (*p*=3.0e-3). 39.1 % of *Dmd*$^{mdx\text{-}\beta geo}$ cells were positive for BrDU compared to 24 % of the corresponding C57Bl/6 controls (*p*=1.0e-2). This statistically significant two-fold increase in BrDU incorporation denotes an exaggerated response to a proliferative stimulus in both dystrophic cells compared to their respective WT controls. Although Dp71 expression was described as enhancing myoblast proliferation [48], we did not observe any negative effect on proliferation in dystrophin-null *Dmd*$^{mdx\text{-}\beta geo}$ cells. On the other hand, this absence of differences between these two genotypes was consistent with the differential gene expression data described earlier.

Significantly decreased chemotaxis of dystrophic myoblasts

In dystrophic myoblasts, several GO categories associated with migration were found to be over-represented in the downregulated gene lists. We therefore assessed, using the Boyden chamber assay, the chemotaxis of dystrophic cells toward sera-rich medium and toward medium containing a cocktail of chemo-attractants (Figure 5b). *Dmd*^{mdx} myoblasts chemotaxis towards both sera-rich and cytokine-containing medium was found to be significantly reduced, with respectively 28 % (*p*=3.8e-2) and 21% (*p*=1.0e-2) cells penetrating through the membrane compared to WT. *Dmd*$^{mdx\text{-}\beta geo}$ myoblasts also showed significantly reduced chemotaxis at 44 % (*p*=5.0e-6) and 54 %, (*p*=7.8e-4), compared to WT controls in serum-rich and cytokines media, respectively.

Altered differentiation of Dmd^{mdx} dystrophic myoblasts

Dystrophic myoblasts showed altered expression of several key genes involved in muscle differentiation (Figure 1c) and GO categories related to differentiation were enriched in downregulated gene lists (Figure4; Table S4). Even though these analyses were performed in proliferating myoblasts, such alterations could indicate a distorted capacity for differentiation in dystrophic cells.

To assess this, differentiation of *Dmd*^{mdx} myoblasts was compared against WT, using a three-dimensional (3D) culture, facilitating interactions closely resembling those occurring in muscles *in situ*.

Spheroids of dystrophic or WT cells (n = 3 per group), were placed in a differentiation medium (t=0) and collected on days 0,2, 4 and 6 to monitor their differentiation. We first established that after 6 days in such condition's spheroids differentiated sufficiently to express myosin heavy chain (Figure S2; supplementary movie https://youtu.be/1axNWeK-Yb0). Changes in differentiation were assessed by qPCR quantification of the expression of *Myh1, Myog and Mymk,* gene markers of myoblast differentiation. Analysis of the time course of expression revealed a significantly altered pattern in *Dmd*^{mdx} cultures. Specifically, *Mymk* (Time: DF = 3, F = 7.520, *p* = 3.4e-2. Group: DF = 1, F = 50.40, *p* = 2.1e-3), *Myog* (Time: DF = 3, F = 9.811, *p* = 1.7e-2. Group: DF = 1, F = 11.72, *p* = 2.7e-2) and *Myh1* (Time: DF = 3, F = 24.97, *p* = 8.0e-4. Group: DF = 1, F = 66.95, *p* = 1.2e-3) were found to have their expression statistically significantly increased (two-way ANOVA) in dystrophic spheroids, when compared to WT (Figure 5c).

Also, in our hands, *Dmd*^{mdx} myogenic cells in 2D cultures formed myotubes within ≈ 5 days, while WT myoblasts required minimum 7 days in the differentiation medium (unpublished), which is in agreement with reports that dystrophic myoblasts differentiate faster [22].

It is worth noting that these increases in *Myh1*, *Myog* and *Mymk* expression in differentiating cells contrast with their expression profiles in proliferating myoblast, where dystrophic cells showed consistently lower expression levels of these markers (Table S1; Figure 1c and Figure S1).

Dystrophic myoblast cell line reproduces transcriptome anomalies found in primary cells

Although multiple replicates of primary myoblasts from the same genotype had similar transcriptome profiles (Figure 1), and primary cultures were free from other cell types, myoblasts isolated from *Dmd*^{mdx} muscle have been exposed to the dystrophic niche and some of the alterations might result from environmental factors. Therefore, we investigated whether alterations found in primary cells also occur in an established myoblast cell line. We used the SC5 (*Dmd*^{mdx}) and IMO (WT) cells, both derived from the H2Kb-tsA58 mice [49] and thus having an identical genetic background. Comparison of RNA-Seq data showed strong segregation of samples according to genotypes (Figure 6a) and a clear dysregulation in gene expression (Figure 5b, Table S5). The SC5 dystrophic cell line transcriptome had significantly more dysregulated genes compared to IMO controls (Table S5) than the primary Dmd^{mdx} myoblasts compared to WT cells (Table S1). Importantly, despite this transcriptome drift expected in cells maintained long-term in culture [50], the key alterations seen in the transcriptome of dystrophic primary cells were also found in the established dystrophic cell line. *Myod1*, *Myog, Mymk, Des* and 69 other genes (Figure 6c; Table S5) were found significantly dysregulated in dystrophic cells, and an overlap in GO (Figure 6c and d; Table S6) demonstrated that the impact of the mdx mutation is present, with 61 GO categories for biological processes being enriched in the downregulated genes lists in both primary and cell line myoblasts carrying the *Dmd*$^{\text{mdx}}$ allele.

Further analysis of these 61 GO categories (Table S6) revealed that all those altered are among the most significantly dysregulated both in terms of adjusted *p*-values and fold enrichment in both primary and established cells, involving very relevant processes and functions, such as "striated muscle tissue development" and "striated muscle cell differentiation" (Figure 6c; Table S6).

Moreover, analysis of overrepresented TF binding sites on promoter regions of the dysregulated genes found transcripts downregulated in the SC5 cells to have significantly higher than background signal for MyoD, MYOG, and TCF12 (Table S3G), in clear agreement with TFBS overrepresented in primary *Dmd*$^{\text{mdx}}$ myoblasts. Likewise, genes upregulated in SC5 did not exhibit statistically significant overrepresentation of the binding signal of any TF (Table S3F).

Finally, in line with these transcriptomic similarities, the dystrophic myoblast cell line exhibited the impaired chemotaxis phenotype (Figure S3), identical to that identified in primary dystrophic myoblasts (Figure 5b).

Human and mouse dystrophic primary myoblasts exhibit corresponding transcriptome changes

Comparison of differential gene expression data from human DMD and healthy primary myoblasts also showed significant transcriptomic alterations with clear segregation between samples according to genotypes (Figure 7a) and a greater number of significantly downregulated genes (334) compared to upregulated ones (86) (Figure 7b, Table S7). This profile was very similar to the primary mouse myoblast data (Figure 1; Table S1).

Comparison of log2 fold changes of significantly dysregulated genes in human DMD myoblasts and their orthologous counterparts in mouse primary *Dmd*$^{\text{mdx}}$ myoblasts revealed that genes significantly downregulated in one species tend to also be downregulated in the other, as shown by more genes in the lower-left quadrant of Figure 7c, compared to other quadrants (Fisher's exact test: p = 2.0e-4). With r values ranging from 0.2357 to 0.4688, depending on which gene populations are compared (Figure 7c and d), the magnitude of gene expression changes between species was equivocal.

However, a comparison of the human GO enrichment for biological processes in the significantly downregulated gene list to its mouse counterpart returned a strikingly similar result, with 61 overlapping categories (Figure 7d and e; Table S8). Of these, 49 also overlap with the categories in the mouse dystrophic myoblasts cell line. Again, the most significantly altered categories (in terms of adjusted *p*-value) that overlap in both species were associated with muscle cell development and differentiation (Figure 7c, Table S8).

When comparing the list of significantly downregulated genes in *Dmd*$^{\mathrm{mdx}}$ versus WT (Table S1) and human DMD versus healthy human myoblasts (Table S8), taking into account only one-to-one orthologs, 41 genes are present in both lists including key myogenic program actors such as *Myog*, *Mymk*, *Myod1*, *Des*, *Smyd1*, *Acta1*, *Actc1* and *Atp2A1*.

Interestingly, other genes of interest found to be dysregulated in primary mouse myoblasts were found to have non-orthologous counterparts dysregulated in human primary DMD myoblasts: *COL11A1*, *COL14A1* and *COL15A1* for *Col2a1*, *Col4a1*, *Col4a2* and *Col8a2* or *MMP2* for *Mmp3*, *Mmp9* and *Mmp10*.

Finally, a three-way comparison of the GO enrichment for biological processes in the downregulated genes for dystrophic primary human myoblasts, primary mouse myoblasts and the dystrophic mouse myoblast cell line showed an important overlap: 49 categories were found enriched in all three datasets, with further 12 enriched in human and mouse primary cells, 12 in mouse primary and mouse cell line datasets and finally 47 categories enriched in both primary human and mouse cell line dystrophic myoblasts (Figure 8a). In the 49 categories enriched in all 3 datasets, many are relevant to the disease and consistent with the cell function anomalies described earlier. Specifically, categories such as “muscle cell differentiation”, “muscle system process”, “regulation of myoblast differentiation” and “regulation of muscle system process” are very significantly enriched in the downregulated gene lists for all datasets (Figure 8b).

Alterations in transcriptomes of human and mouse dystrophic myoblasts are strikingly analogous, with downregulation of gene expression predominating in both, reduction in key markers of the muscle program and relevant common GO categories being enriched. Importantly, our data provide a molecular underpinning for previously reported abnormalities in proliferation, migration and differentiation of human DMD myoblasts [51–54].

Metabolic pathway alteration in DMD primary myoblasts

Skeletal muscle metabolism is a significant variable [33], as metabolic dysfunction can impair skeletal muscle regeneration, and DMD affects cellular energetics in muscle progenitors [34]. Therefore, we investigated the metabolic alterations in human DMD myoblasts. To this end, we built a dystrophic genome-scale metabolic model, following our previous pipelines for generating context-specific metabolic models using omics data [55]. Figures 9 and S7 illustrate the metabolic activity fold change (expressed in log2FC) across reactions in the enzyme-constrained human metabolic model. We differentiated the metabolic pathways into upregulated and downregulated groups (detailed results are shown in Table S11). We found a significant change in the rate of glycolysis/gluconeogenesis (log2FC = 4.8), leukotriene metabolism (log2FC = 4.754), propanoate metabolism (log2FC = 5.657), mitochondrial beta-oxidation of branched-chain fatty acids, odd-chain fatty acids , and di-unsaturated fatty acids (n-6) (log2FC = -1.187 , log2FC = -0.8295 and log2FC = -0.655) (Figure 10a).

Similarly, the activity of phosphoglycerate mutase 2 and 2-phospho-D-glycerate proteins is significantly increased in the glycolysis/gluconeogenesis metabolic pathway (Figure S7, Supplementary Table S11). The glycolytic enzyme, phosphoglycerate, catalyses the interconversion of 3-phosphoglycerate and 2-phosphoglycerate in the presence of 2,3-bisphosphoglycerate [56]. The glycosphingolipid biosynthesis-lacto and neolacto series pathways are also downregulated in DMD (log2FC = -0.49), decreasing the production of type I B glycolipid, sialyl-3-paragloboside metabolites.

Mitochondrial propanoate metabolism is observed to have upregulated activity in DMD cells (log2FC = 5.657) (Figure 9) indicating an increase in the activity of propionyl-CoA synthetase in mitochondria, which can impair myogenic differentiation [57].

DMD is characterised by the decrease of mitochondrial aconitase (ACO2) [58], and the downregulation of isocitrate hydro-lyase citrate cycle metabolic reactions (r0426) in the TCA cycle indicates a significant decrease of the aconitase metabolite in DMD myoblasts. This suggests that the interconversion of citrate to isocitrate as part of the citric acid cycle is carried out at a reduced rate, therefore directly impairing carbohydrate and energy metabolism. We also found that the upregulation of glycine-N-acetyltransferase reaction in Phenylalanine metabolism increases the production of phenylacetyl-CoA and glycine in DMD myoblasts. The upregulation of phenylalanine in skeletal muscle is associated with decreased mTOR activity, a key regulator of cell growth and anabolism [59].

Alterations in the activity of other mitochondrial pathways and reactions were also found (Figure 9a and b respectively). Further reaction-level alterations in pyruvate metabolism, glycolysis/gluconeogenesis, transport reactions, glycosphingolipid biosynthesis-lacto and neolacto series metabolic pathways are shown in Supplementary Figure S7.

Thus, these molecular and fucntional myoblast abnormalities identified across mouse and human dystrophic cells and in cell lines are the consequence of DMD gene mutations.

Discussion

DMD presents in muscle stem cells, where the loss of dystrophin affects asymmetrical cell divisions [60]. Subsequently, the absence of dystrophin during myotube differentiation causes typical dystrophic abnormalities such as altered calcium homeostasis and creatine kinase leakage [4]. We hypothesised that myoblasts originating from dystrophic stem cells, which give rise to myotubes, are also affected. Indeed, we demonstrate here for the first time that, in proliferating human and mouse myoblasts, the absence of *DMD* gene expression results in major abnormalities. Our data combining global RNA-Seq and functional analyses demonstrate that DMD directly affects myoblasts.

The key alterations concerned proliferation, chemotaxis, and differentiation. Importantly, synchronisation of these three processes, involving exit from the cell cycle, migration to the site of damage, activation of the skeletal muscle-specific genes and cell fusion, is essential for muscle development and regeneration. Ultimately, myoblasts are the effector cells of muscle growth and repair, and it is the failure of muscle regeneration that drives DMD progression.

These defects are cell autonomous rather than caused by the inflammatory environment of the dystrophic niche because they persist in the dystrophic cell line maintained long-term in culture: established cells reproduced the key transcriptomic anomalies and were described before to have functional alterations found in primary cells [61].

Moreover, alterations are shared between mouse and human DMD myoblasts, despite the significant heterogeneity within human samples [17,62]. Therefore, these dystrophic anomalies manifest irrespective of genetic backgrounds and across species, which confirms their significance. Furthermore, altered proliferation, migration and differentiation in DMD myoblasts have been reported [51–54] and our data provide the molecular underpinning for these abnormalities.

DMD pathology being intrinsic to the myoblast has been proposed previously [20] and there has been growing evidence that *DMD* mutations cause a range of cell-autonomous abnormalities in human and mouse myogenic cells and myoblasts, which affect cell division, differentiation, energy metabolism and signalling [22–24,24,31,31,60,63–66]. Interestingly, *Dmd*$^{\mathrm{mdx}}$ cell migration found reduced under physiological stimuli (this work) can be increased in the inflammatory environment [31]. In fact, altered proliferation and migration resulting in highly metastatic phenotypes, have been associated with the loss of Dp427 in tumours featuring myogenic differentiation [67].

Our team recently demonstrated that *DMD* mutations evoke marked transcriptome and miRNome dysregulations early in human muscle cell development [17]. In that study, expression of key coordinators of muscle differentiation was dysregulated in proliferating dystrophic myoblasts, the differentiation of which was subsequently also found to be altered, in line with the mouse cells studied here (Figure 5c).

A significant number of downregulated transcripts in dystrophic myoblasts are controlled by the same TFs, most notably MyoD and MYOG. Given that MYOG itself is regulated by MyoD, the significant downregulation of *Myod1* expression found here appears to be the key trigger mechanism of the dystrophic abnormality in myoblasts: the lower levels of *Myod1* transcript strongly correlate with downregulated expression of genes controlled by this TF, and which are key coordinators of skeletal muscle repair. Consequently, altered expression of myogenic regulatory factors in dystrophic myoblasts could have multiple consequences. Indeed, complete *Myod1* ablation in *Dmd*^{mdx} has been shown to exacerbate the disease due to a diminished capability for muscle regeneration [68,69]. Downregulation of MyoD*,* which inhibits the cell cycle, could explain the increased proliferation in dystrophic cells. The *Myod1-Mymk-Mymx* (Myomaker/ Myomixer) axis altered here was found to determine myotube formation [70]. Given that *Pax3* inhibits myogenic differentiation of myoblasts [71], its downregulation in dystrophic cells could also contribute to this accelerated differentiation pattern observed here.

GO categories concerning calcium homeostasis and signalling, known to be altered in dystrophic muscles across species, were also found altered in dystrophic myoblasts: calsequestrins 1 and 2 levels being significantly downregulated, in line with previous findings in the dystrophic muscle [7,45] and cell lines [61,64].

Given that Dp71 dystrophin is found in undifferentiated myogenic cells [30], and that in development shorter dystrophins have been associated with proliferation and migration, and long isoforms with terminal commitment [72], we hypothesized that eliminating expression of Dp71 may exacerbate dysfunctions in myogenic cells. Surprisingly, we found that both *Dmd*^{mdx} and *Dmd*$^{mdx\text{-}\beta geo}$ cells had similar abnormalities and, contrary to Dp71 overexpression increasing myoblast proliferation [48], BrdU incorporation in dystrophin-null myoblasts was still significantly increased compared to WT. Interestingly, *Dmd*^{mdx} myoblasts, having a point mutation in exon 23, expressed significantly lower levels of Dp71 (Figure S6), whose expression is driven by a promoted located over 40 exons downstream of the mutation. But whether this downregulation is sufficient to mimic its total loss is unknown.

Combined, these data bring to light the significance of full-length dystrophin defects in undifferentiated muscle cells, the consequences of which correspond to the impaired muscle regeneration occurring in this disease.

Clearly, the important question is the mechanism altering the myoblast phenotype. Dp427 in satellite cells appears to control asymmetrical cell division [60], which might suggest an interaction problem also in myoblasts.

However, even healthy myoblasts do not express Dp427 protein at levels detectable by Western blotting: an observation that contributed to the belief that myoblasts are not affected by *DMD* mutations. Although our attempts at immunolocalization in unsynchronised primary myoblasts failed to detect Dp427 (Figure S4), a precise spatio-temporal requirement for small amounts of full-length dystrophin, analogous to its role in satellite cells [60] or at neuronal synapses [73] is a possibility that should be studied. Importantly, WT myoblasts express the full-length transcript, which is depleted in dystrophic cells. It is worth noting that this 14 kb mRNA, which transcription time may be as long as 16 h [3], is produced in rapidly dividing myoblasts. Its expression is therefore unlikely to be meaningless. Indeed, downregulation of full-length dystrophin occurs across various malignancies and is associated with alterations of molecular pathways that were identical with alterations found in Duchenne muscles. Moreover, low DMD gene expression in tumours was associated with poor patient survival (https://www.biorxiv.org/content/10.1101/2022.04.04.486990v3). Clealry, dystrophin mis-expression is far more consequenctial and can affect many more cells and tissues than previously understood.

Is it possible that loss of the full-length dystrophin expression may trigger a mechanism not involving its protein product? Considering the increasing number of human pathologies caused by RNA, including another dystrophy – *dystrophia myotonica* [74], it is not inconceivable that loss of a large 14 kb transcript made up of 79 exons may trigger a novel RNA-mediated disease process [75]. Abnormalities in *Dmd*$^{\mathrm{mdx}}$ cells, that harbour just a point mutation, indicate that the patho-mechanism does not require large *Dmd* gene rearrangements [76]. Yet, improvements resulting from the expression of mini/micro dystrophins do not support the requirement for the entire 14 kb transcript or a toxicity of mRNA breakdown products generated *via* nonsense-mediated decay. However, the impact of premature dystrophin transcript termination on the downregulation of other genes [77] cannot be excluded.

A more likely explanation involves alterations of epigenetic regulation, a mechanism of increasing importance in DMD: The absence of dystrophin/DAPC in satellite cells leads to aberrant epigenetic activation, which impairs functions of the newly generated cells. This dystrophic SC division defect has been linked to polarization problem due to MARK2 mis-interaction [78] combined with β-syntrophin abnormalities [79,80]. Downregulation of β-syntrophin, a DAPC member, results in impaired polarization of its interactor - p38γ. This, in turn, increases CARM1 phosphorylation and reduces *MYF5* activation by PAX7 in in the daughter cell due for myogenic differentiation [81]. Furthermore, dystrophin anchors nNOS [82], which becomes mis-localised in dystrophic cells. This results in decreased nitric oxide-dependent S-nitrosylation of HDAC2 [83] and higher deacetylase activity that has been shown to be involved in the progression of muscular dystrophy [84].

Thus, loss of the full-length dystrophin in muscle stem cells does not abrogate myogenic cell divisions but causes significant abnormalities. The descendant myoblasts appear to be harbouring somatically heritable epigenetic changes analogous to genomic imprinting [85] and themselves might manifest significant epigenotype abnormalities [86].

Indeed, our *DMD* knockdown and rescue experiments in skeletal muscle progenitor cells [17] showed that phenotypic changes at day 17 were the consequences of some earlier events that occurred at day 10 and that some abnormalities might not be reproduced nor alleviated after crossing a specific checkpoint.

The data here indicate that epigenetic changes in dystrophic primary myoblasts may be present, as amongst the significantly altered genes *Hist2h2ac*, *Hist1h2ag*, *Hist1h2ah*, *Hist1h1a, Smyd1 and Hmga1* gene products are involved in chromatin modifications or belong to the GO category "negative regulation of gene expression, epigenetic". Methylated histone H3 lysine 4 (H3K4) is a key epigenetic signal for gene transcription. H3K4 methylation is mediated by several methyltransferases, including muscle-active *Smyd1* [87], found among the top downregulated transcripts in dystrophic myoblasts. Histone methylation can be reversed by histone demethylases, of which Lysine-Specific Histone Demethylase 1A (LSD1 encoded by *Kdm1a*) is an important muscle enzyme [88]. The network of interactions between genes in this aforementioned GO category (Figure S5, Table S9) showed a clear interface between the *Kdm1a* node and significantly downregulated histone genes. LSD1 is involved in controlling *Myod1* expression [89], which we found significantly downregulated in dystrophic myoblasts. Importantly, treatment of Dmd^{mdx} mice with histone deacetylase inhibitors (HDACi) promoted myogenesis [90]. Epigenetically, HDACi upregulate *Myod1* [91] and therefore would counteract its decreased expression and the resulting downregulated expressions of genes controlled by this TF, which we described here.

We postulate that, in dystrophic myoblasts, epigenetic dysregulation of *Myod1* expression causes a pathological cascade of downregulated transcriptions of a range of genes controlled by MyoD, with functional consequences for muscle regeneration.

If it is the absence of dystrophin in myogenic cells that determines their fate, developmental muscle abnormalities should occur. This is indeed the case: asymptomatic DMD patients already have transcriptomic alterations [10] and myogenesis in Dmd^{mdx} embryos is severely disrupted, with myotube hypotrophy, reduced myotube numbers and displacement defects [16]. This developmental abnormality continues in adult muscles during regeneration.

Altogether, our data identify a continuum, where mutations disrupting expression of full-length dystrophin cause SC division abnormalities impacting myoblast generation but also imprinting these cells with functionalities further reducing muscle regeneration. And as dystrophin is needed at the myotube stage for the initial assembly of the DAPC and subsequent formation of viable myofibres [4], dystrophinopathy results in contraction-induced injury in mature muscle [5]. Thus, the vicious circle of disease is closed with both degenerative and regenerative abnormalities contributing to DMD progression (Figure 10).

Such a scenario explains the apparent contradiction, where removal of dystrophin and/or DAPC in fully developed myofibres does not result in dystrophic muscle damage [5,6]. It would be the case if, once formed in a healthy muscle, DAPC remains stable even if dystrophin is subsequently lost, as indeed have been demonstrated [6].

Moreover, as the efficacy of exon skipping and gene targeting methods is much higher in proliferating cells than in myofibres, all outcomes of these treatments could arise from dystrophin re-expression in myoblasts, which later differentiate into myotubes with the functional DAPC.

Findings described here agree with the existing data that loss of dystrophin expression disrupts many downstream processes. These processes offer good targets for therapeutic interventions that are not constrained by the causative mutation [92–94]. Importantly, adjustments made in dystrophic myoblasts can reduce or even prevent occurrence of dystrophy. For example, upregulation of Jagged 1 can counteract damage in muscles without any dystrophin [8] and corrections to COUP-TFII [95], EGFR-Aurka and Ghrelin expression [96] can reduce muscle damage.

Given that these pathways are active in myoblasts and the proteins involved are structurally incompatible with substituting the scaffolding properties of dystrophin, these findings further challenge the role of dystrophin in myofibre sarcolemma stabilization as the key pathological alteration in DMD.

Interestingly, the metabolic analysis indicated a significant alteration in key metabolic pathways in DMD myoblasts, which were in line with alterations in the rate of glycolysis/gluconeogenesis, tricarboxylic acid cycle, fatty acid activation, and propanoate metabolism previously found in DMD patients (as previously reviewed [97]). Clearly, the DMD impact on metabolism is an early and widespread disease manifestation, with abnormalities presenting already in the embryonic development[17] and present in myoblasts[47] (and this work), in differentiated muscle and also in dystrophic brains [98]. As an increase in energy demand is observed in DMD muscle, the upregulation of the glycolysis/gluconeogenesis metabolic pathway suggests the upregulation of glucose metabolism-related enzymes, including hexokinase (D-glucose:ATP) and pyruvate kinase, which compensates for the energy demand [99]. These changes are also compensated by other metabolic alterations in mitochondrial pathways and reactions, e.g. the downregulation of mitochondrial beta-oxidation of branched-chain fatty acids, odd-chain fatty acids, and di-unsaturated fatty acids (n-6)

[100]. Notably, these metabolic adaptations are activated in dystrophic myoblasts and not just myofibres, which could be easier explained by increased energy demands.

The synthesis of ATP and phosphocreatine is catalysed by creatine kinase in a reversible mechanism [101,102]. Therefore, creatine kinase, significantly downregulated in Arginine and proline metabolism of mitochondrial centre (Figure 10b) signifies the reduction of ATP production in DMD myoblasts [103]. The ATP dysfunction at the mitochondrial level induces several patho-physiological events and should exacerbate dystrophinopathy [102].

The mitochondrial leukotriene metabolism is found to be significantly elevated in DMD myoblasts, consistently with the fact that muscle can produce leukotrienes, which are implicated in inflammation and contribute to muscle weakening [104]. Furthermore, the observed upregulation in propanoate metabolism leads to the accumulation of propionyl-CoA and associated metabolites in plasma, and increases the levels of propionyl-CoA and protein propionylation, which can impair myogenic differentiation in human myoblasts [57].

Glucose-6-phosphate dehydrogenase is known to contribute to the regulation of glucose uptake in skeletal muscle [105]. The downregulated fold change of glucose 6-phosphate dehydrogenase (G6PDH2cNo1) suggests that the concentration of glucose is significantly altered in DMD myoblasts. The reduction in the glucose level could impair the differentiation of skeletal myoblasts through the activation of a pathway that targets the enzymatic activity of SIRT1 [106].

Our findings here, combined with the other data, provide compelling foundation for the call to re-evaluate the established belief on the pathogenesis of DMD. Such reconsideration is important because most current therapeutic approaches aim at dystrophin restoration in differentiated myofibres and are often conducted in the advanced-stage disease, with very limited regenerative muscle potential. Despite decades of intensive research and numerous clinical trials, none of the candidate treatments delivered disease-modifying results [107]. Part of the problem is immune responses to re-expressed dystrophin [108], which need to be tackled [109] or prevented. However, dystrophin re-expression using new technologies [110] allowing re-targeting dystrophin to myoblasts and satellite cells in younger patients or, better still, in newborns able to develop neonatal tolerance to dystrophin, could produce effective therapies for this devastating disease.

Materials and methods

Animals

Male C57BL/10ScSn-*Dmd*^{mdx}/J, C57BL/10ScSnJ, C57BL/6-DmdGt(ROSAbgeo)1Mpd/J (*Dmd*$^{mdx\text{-}\beta\text{geo}}$) and C57BL/6J eight week old mice were used in accordance with institutional Ethical Review Board and Home Office (UK) Approvals. All mice were maintained under pathogen-free conditions and in a controlled environment (12-hour light/dark cycle, 19-23°C ambient temperature, 45-65 % humidity). For environmental enrichment, tubes and nesting materials were routinely placed in cages. The genotypes of all experimental animals were confirmed by PCR.

The C57BL/10 and C57BL/6 strains derived from a common origin [111] and it has been demonstrated that the mdx mutation on the C57BL/6 background shows the same pathology as the original C57BL/10 strain [112]. Nevertheless, for RNA-Seq experiments, mixed background animals were generated to facilitate the direct comparison between *Dmd*$^{\text{mdx}}$ and *Dmd*$^{\text{mdx-}\beta\text{geo}}$ transcriptomes. For this, *Dmd*$^{\text{mdx}}$ males were paired with C57BL/10 females and C57BL/6 males were paired with *Dmd*$^{\text{mdx-}\beta\text{geo}}$ females. The resulting *Dmd*$^{\text{mdx/WT}}$ females and *Dmd*$^{\text{mdx-}\beta\text{geo}}$ males were then bred together. The resulting *Dmd*$^{\text{WT}}$ males were used as controls and bred with the *Dmd*$^{\text{mdx/mdx-}\beta\text{geo}}$ females. The next generation *Dmd*$^{\text{mdx}}$ and *Dmd*$^{\text{mdx-}\beta\text{geo}}$ males were used as the dystrophic groups. For the subsequent functional pairwise analyses, *Dmd*$^{\text{mdx}}$ were compared against C57BL/10 and *Dmd*$^{\text{mdx-}\beta\text{geo}}$ against C57BL/6 mice.

Primary myoblast extraction and culture

Gastrocnemii from 8-week-old male mice (during the active disease period) were used for myoblast extraction and culture. *Gastrocnemius* was chosen as it is considered a fast muscle with predominantly IIB fibres [113] and therefore more prone to dystrophic changes and producing a relatively homogenous population of myoblasts. Briefly, muscles were dissected free of fat and connective tissue before enzymatic digestion by 0.2 % type IV collagenase (Sigma, C5138) in Dulbecco's Modified Eagles' Medium (DMEM, Gibco 31885-023) for 90 min at 37°C, 5 % CO_2. The digested muscles were then rinsed in plating medium (10 % horse serum, Gibco 26050-088; 0.5 % chicken embryo extract, Seralab CE-650-J; 100 units penicillin / 0.1 mg streptomycin per mL, Sigma P0781; in DMEM, Gibco 31885-023) incubated at 37°C, 5 % CO_2. Digested muscles were then disrupted by successive passages in 50 mL, 25 mL and 10 mL serological pipettes. The freed muscle fibres were transferred to a dish containing plating medium.

The dish was then placed under a stereo microscope and 200 live fibres were transferred to another dish containing plating medium. This procedure was repeated 2 more times until 150 fibres were transferred to a third dish. 120 live fibres were then transferred to a tube containing proliferating medium (20 % foetal bovine serum, Gibco 10500-064; 10 % horse serum, Gibco 26050-088; 0.5 % chicken embryo extract, Seralab CE-650-J; penicillin / streptomycin, Sigma P0781; in DMEM, Gibco 31885-023). The resulting suspension of muscle fibres was then disrupted by passing it through an 18-gauge needle 10 times before passing the resulting solution through a 40 µm cell strainer (BD Falcon 352340).

The strained cell suspension was transferred to a collagen I (Sigma C8919) coated cell culture dish and proliferating medium was added to obtain an appropriate volume for the dish. The cells were then cultured at 37°C, 5% CO_2 humidified atmosphere and used for assays and experiments. The purity of myoblast cultures was confirmed by enumeration of cells immunofluorescently stained for MyoD (Supplementary Figure 8). Cells were detached from dishes using Accutase (Biowest L0950). Myoblasts were never passaged more than once and cells from the same passage for dystrophic and control genotypes were used for comparabilty.

Myoblasts cell lines

The SC5 (mdx) and IMO (WT) cell lines were derived from the leg muscle of the H2Kb-tsA58 line [49]. Cells were cultured in DMEM supplemented with 20% FCS, 4mM L-glutamine, 100 unit/ml penicillin, 100 µg/ml streptomycin and 20 unit/ml murine γ-interferon (Invitrogen) at 33°C, 5% CO_2 humidified atmosphere. When cells reached 95% confluence, they were cultured as primary cells in KnockOut DMEM (Invitrogen) supplemented with 10% v/v Knockout Serum Replacement (KSR, Invitrogen), 5% v/v Donor Horse Serum (DHS, Sera Labs) and 2mM L-glutamine at 37°C.

RNA extraction

Myoblasts isolated from gastrocnemii from 3 individual mice per experimental group were treated as biological replicates. Total RNA was extracted from Dmd^{mdx}, $Dmd^{mdx\text{-}\beta geo}$ and corresponding wild-type myoblasts using RNEasy Plus Universal mini kits (Qiagen 73404). Briefly, cells were washed 2 times with warm Dulbecco's phosphate buffered saline DPBS, Gibco 14190144) before lysis by applying QIAzol directly to the freshly washed cells. Lysate was then homogenised by passing it through a 25-gauge needle 20 times. Samples were then processed according to the kit manufacturer's instructions. RNA quality and concentration were measured using a NanoDrop 1000 Spectrophotometer (Thermo Scientific). RNA integrity was assessed using electrophoresis of 100 ng of total RNA in a 1 % agarose gel (Sigma A4718) in TRIS-acetate-EDTA (TAE) buffer or using an automated capillary electrophoresis system (2100 Bioanalyzer Instrument G2939BA, Agilent) using a kit assay (Agilent RNA 6000 Nano Kit 5067-1511, Agilent).

RNA Sequencing

Total RNA samples (n=3 per group) were processed by TheragenEtex (Republic of Korea) using an Agilent Bioanalyzer 2100 for quality assessment of samples with a threshold of 7.0 for the RNA integrity number (RIN). An Illumina TruSeq stranded total RNA kit was used to generate libraries following a ribodepletion step using a Ribo-Zero Human/Mouse/Rat kit. Libraries were sequenced in a paired-end 100 bp run using an Illumina HiSeq 2500 sequencing platform.

Raw reads were quality assessed using fastQC [114] and reads were trimmed using trim-galore [115] with parameters “--illumina -q 20 --stringency 5 -e 0.1 --length 40 --trim-n” to remove adapter sequence and low-quality sequence tails. Reads were mapped to the GRCm38 *Mus musculus* genome from Ensembl using the STAR universal RNA-Seq aligner [116] with parameters “--outSAMmultNmax 300 --outSAMstrandField intronMotif”. Output mapping files were processed and filtered to remove non-mapping reads with mapping quality less than 20 using samtools [117].

The DESeq2 package [118] in R [119] was used to perform differential gene expression analysis. Gene models were taken from Ensembl version 91, and read counts over unique genes were quantified using the *summarizeOverlaps()* function in the GenomicAlignments package [120] using parameters ‘mode = “Union”, singleEnd = FALSE, ignore.strand = FALSE, fragments = FALSE, preprocess.reads = invertStrand’. *P* values were adjusted for multiple comparisons by using the Benjamini and Hochberg correction [121]. Significantly differentially expressed genes were identified based on a fold-change of 2-fold or greater (up- or downregulated) and an adjusted *p*-value < 5.0e-2. An additional filter was put in place to remove genes where the mean normalised Fragments Per Kilobase Mapped (FPKM) was < 1 for both conditions to avoid changes in low abundance transcripts. GO enrichment analysis was conducted using the clusterProfiler package [122] in R [119].

REVIGO [123] was used to reduce the redundancy of GO enrichment data to rationalise the categories being compared in figures. The default “SimRel” semantic similarity measure with a 0.4 threshold cut-off was used. When filtering GO categories for redundancy, the mouse UniProt database was used for all analyses, except when analysing the list of GO categories enriched in both human and mouse primary datasets, in which case the human UniProt database was used. STRING [124] was used to explore and visualize interaction networks. Only interactions present in databases for relevant species or experimentally determined were used.

Regulatory regions of the differentially expressed genes (listed in Tables S2, S3, S5, and Table S3H), defined as the region 1 Kb upstream or downstream of the transcription start site (TSS) of the gene, were analysed for overrepresentation of binding sites of transcription factors (TFs). The binding signal was analysed using the seqinspector tool (http://seqinspector.cremag.org, [125] and publicly available ChIP-Seq data [46]. The overrepresentation was assessed by comparing the lists of tested genes with 1000 randomly selected gene promoters (Mus musculus reference genome mm9) Ensembl 75 gene symbols. TF signal was considered enriched if Bonferroni-corrected p-value returned by seqinspector was < 5.0e-2.

RNA-Seq data have been deposited in the ArrayExpress database at EMBL-EBI under accession number E-MTAB-10322 for the primary mouse myoblast samples (https://www.ebi.ac.uk/arrayexpress/experiments/E-MTAB-10322) and accession number E-MTAB7287 for SC5 and IMO myoblast cell line samples (https://www.ebi.ac.uk/arrayexpress/experiments/E-MTAB-7287).

Human primary adult myoblast RNA-Seq data

The collection of primary myoblasts was established as part of the medical diagnostic procedure. A signed and informed consent was obtained by the Cochin Hospital cell bank/Assistance Publique-Hôpitaux de Paris for each patient to collect, establish, and study primary cultures of cells. This collection of myoblasts was declared to (i) legal and ethical authorities at the Ministry of Research (declaration number 701, modified declaration number 701–1) *via* the medical hosting institution (Assistance Publique-Hôpitaux de Paris) and to (ii) the 'Commission Nationale de l'Informatique et des Libertés' (declaration number 1154515). RNA-Seq data from human dystrophic (duplication exons 3–26, deletion exons 8–43, and stop exon 7) and healthy primary myoblasts were generated and analysed as described [17]. Raw RNA-Seq data have been deposited in the ArrayExpress database at EMBL-EBI under accession number E-MTAB-8321 (https://www.ebi.ac.uk/arrayexpress/experiments/E-MTAB-8321). This RNA-Seq data was then used to analyse the metabolic changes in DMD myoblasts.

The complete fold change values for the human DMD and healthy samples estimated using the DESeq2 package (as described in the RNA Sequencing section) were further used to reconstruct the DMD-specific Genome-Scale Metabolic Model (GSMM), as described below. The genes with NaN fold change were unperturbed for the metabolic analysis.

Reconstruction of the genome-scale metabolic model

The myoblast-specific metabolic model was constructed using an extensively curated GSMM of human metabolism [126]. As significant enzymatic changes are observed in DMD [127], and in order to fully take into account enzymatic activity, an enzyme-constrained Human model, built with GECKO version 1.0 [128] was used.

Using the previously developed method for building context-specific models [129], the fold change value of RNA-Seq data was integrated into GSMM to constrain the myoblast-specific metabolic network [130]. The idea is to constrain the base enzyme constrained human metabolic model with upper and lower bounds on metabolic reactions depending on the fold change value of gene expression data, also taking into account the role of each gene in each reaction [131]. Based on previously reported increased or decreased enzymatic activities stated in the literature, the upper and lower bound of the metabolic reactions associated with the enzymes were further constrained.

The context-specific model was then solved using flux variability analysis (FVA) to obtain the minimum and maximum flux rate for each reaction, satisfying the given constraints. The FVA was performed by solving a 2n linear programming problem on the constrained metabolic model using the COBRA toolbox [132] and the gurobi solver. The full details of the metabolic modelling framework are reported in the Supplementary File 1.

cDNA synthesis and qPCR analysis

Total RNA samples were converted to cDNA using SuperScript VILO cDNA Synthesis Kit (Invitrogen 11754050) as per manufacturer instructions.

qPCR reactions were run in duplicates using 25 ng of cDNA per reaction with Precision Plus Mastermix (Primer Design PPLUS-LR), forward and reverse primers synthesized by Eurofins (Table S10) and DEPC treated water (Fisher Bioreagents BP561) as per manufacturer instructions, in 96 well plates using an Applied Biosystem ViiA7 RT-PCR instrument, and expression quantified using the ΔΔCT method.

Cell proliferation assay

Primary myoblasts were seeded in 10 cm diameter dishes (Sarstedt 83.3902) coated with Collagen I (Sigma C8919) at 30 % confluency in proliferation medium, as above and left to attach for 2 hours before adding bromodeoxyuridine / 5-bromo-2'-deoxyuridine (BrDU, Invitrogen B23151) to a final concentration of 75 µM and left to proliferate for 6 hours. Cells were then rinsed with warm DPBS, detached using Accutase (Biowest L0950) and fixed using ice cold ethanol. Samples were left at -20°C over-night and then analysed by flow cytometry. Fixed cells were submitted to an acid wash (2M HCl, 0.5 % Triton X-100) for 30 min at room temperature, washed in PBS and the remaining acid was neutralized using a borate buffer (pH= 8.5). Cells were then stained in 200 µL of PBS (0.5 % Tween 20) with 1 µg of Anti-BrDU FITC conjugated antibody (BD 556028) or an FITC conjugated isotype control for 30 min at room temperature. Cells were then washed in HEPES buffer (pH= 7.4) and resuspended in PBS before processing using a FACScalibur system.

Boyden chamber chemotaxis assay

Primary myoblasts from dystrophic and WT mice were treated for 2 hours with proliferating medium complemented with 10 $\mu g.mL^{-1}$ mitomycin C (Fisher Bioreagents BP2531) to prevent proliferation from confounding the results of the assay. Cells were then rinsed with warm DPBS twice to remove excess mitomycin C. Each insert (Sartstedt 83.3932.800) was seeded with 10 000 myoblasts in serum-free medium while the wells were filled with either proliferating medium or serum-free medium complemented with 10 $ng.mL^{-1}$ FGF-b (R&D Systems 3139-FB), IGF-I (R&D Systems 791-MG) and HGF (R&D Systems 2207-HG). Cells were left for 12 hours before fixation in buffered formalin (Sigma HT501128) and crystal violet staining for cell counting and spectrophotometer measurements.

Cell differentiation assay

Myoblasts were used to generate spheroids as such a culture provides an environment that facilitates myogenic differentiation due to a 3D structure improving physical interactions, differentiation and fusion of myoblasts [133–136]. One million myoblasts per genotype and per mouse were pelleted at 300g for 5 minutes in 15 mL centrifuge tubes before pellets were transferred into individual wells of a 6-well plate containing 50 % proliferation medium (20 % foetal bovine serum, Gibco 10500-064; 10 % horse serum, Gibco 26050-088; 0.5 % chicken embryo extract, Seralab CE-650-J; penicillin / streptomycin, Sigma P0781; in DMEM) and 50 % DMEM (Gibco 31885-023) and cultured for 24 hours. Then cells were placed in 25 % proliferation medium with 75 % DMEM for 24 hours and finally in the differentiation medium (2 % horse serum, Gibco 26050-088; penicillin / streptomycin, Sigma P0781; in DMEM). Introduction to differentiation medium was considered t=0 and differentiation was allowed for 6 days.

At the collection time, spheroids undergoing differentiation were rinsed in DPBS and collected in 1 mL of Qiazol solution before freezing for subsequent processing. On thawing, spheroids were disrupted using progressively smaller gauge needles (19, 21, 23 and 25 gauge) and then processed as *per* the RNA extraction section. *Mymk* was chosen as a marker of myoblast fusion and therefore entry into the final stages of differentiation [137] and *Myog* and *Myh1* as robust markers of late stage myogenic differentiation [138].

Immunolocalisation with confocal microscopy

Muscles (tibialis anterior) frozen in liquid N_2 chilled-isopentane in cryo-embedding matrices (Cellpath KMA-0100-00A) were allowed to equilibrate to -20 °C in the cryostat chamber. Cryosections (10 µm) were cut and attached to poly-L-lysine coated slides (Thermo Scientific J2800AMNZ). Sections were allowed to air-dry before fixation and staining. Myoblasts were seeded at 10 000 per collagen-coated coverslip in a 24 well plate (Sarstedt 83.1840.002 and 83.3922) and left to adhere for 12 hours before processing. Spheroids having undergone the differentiation process were frozen in embedding medium and 10 µm sections were cut, as previously described.

Both muscle sections and cultured myoblasts were then processed identically. They were fixed in 10 % neutral buffered formalin (Sigma-Aldrich HT501128) at room temperature for 10 minutes and washed 3 times in PBS containing 0.1 % v/v Triton X-100 (Sigma-Aldrich X100), blocked for 30 min using 10 % v/v chicken serum (Gibco 16110082) in PBS-Triton then incubated for 90 minutes under agitation in primary antibody solution: anti dystrophin (Developmental Studies Hybridoma Bank MANDYS1 clone 3B7 cell culture supernatant) 25 % v/v antibody or anti Myosin-4 (Invitrogen, 14-6503-95) 1µg.mL^{-1}, 10 % v/v chicken serum in PBS-Triton. Samples were then washed one time in PBS-Triton then incubated in secondary antibody solution (Invitrogen A-21200) with 10 µg.mL^{-1} antibody, 10 % v/v chicken serum and DAPI 300 nM (Invitrogen D1306) in PBS-Triton for 1 hour followed by 2 washes in PBS-Triton then PBS and mounted using an anti-fading mounting medium (Thermo Scientific TA-006-FM). Omitting primary antibodies in the reaction sequence served to confirm the specificity of the signal.

Samples were examined with a confocal laser-scanning microscope (LSM 880; Zeiss, Oberkochen, Germany) using a Plan Apochromat, 63x DIC oil objective (NA 1.4) (pixel size 0.13 µm) objective. Images were acquired using sequential acquisition of the different channels to avoid crosstalk between fluorophores. Pinholes were adjusted to 1.0 Airy unit. In all cases where multiple images were captured from the same immunohistochemical reaction, laser power, pinhole, and exposure settings were captured once on sample from a representative control section and maintained throughout imaging. Images were processed with the software Zen (Zeiss) and exported into tiff images for figure generation or WMV for video exporting. Only brightness and contrast were adjusted for the whole frame, and no part of any frame was enhanced or modified in any way.

For immunodetection of MyoD, freshly isolated cells were re-plated on coverslips in growth medium and allowed to grow to 70-80% confluence. After rinsing twice with PBS (w/o calcium and magnesium) cells were fixed in a 4% w/v paraformaldehyde solution (PFA) in PBS for 10 min at room temperature (RT), permeabilized in PBS with 0.1% Triton X-100 for 5 min and blocked in a 5% v/v goat serum (GS, Normal Goat Serum, S-1000, Vector Laboratories IVD) in PBS for 1 h at RT. Cells were incubated with MYOD monoclonal antibody (MA5-12902 ThermoFisher Sci.) diluted 1:100 in the blocking buffer at 4°C overnight. The secondary antibody (Alexa Fluor 594 goat anti-Mouse, ThermoFisher A11032, 1:1000 in 5% GS in PBS) was applied for 1 h at RT in the dark. Cells were rinsed in PBS and washed twice for 5 min with 1% GC with slow agitation. Then cells were incubated with Hoechst (1:1000 from stock solution 10 mg/ml) for 10 min at RT in the washing buffer. Finally, cells were rinsed and washed two times for 5 min with PBS with agitation. The coverslips were mounted onto microscope slides in Glycergel Mounting Medium (VectaShield®, Vector Laboratories) prior to imaging. Images were obtained using a confocal microscope (Zeiss Spinning Disk Confocal Microscope Axio Observer Z.1) and image analysis was performed using ImageJ software.

Statistical analysis.

Student's unpaired t-test was used for comparisons between two data groups. Two-way ANOVA was used to determine if there was any statistically significant difference between groups and time points in the differentiation assay and Fisher's LSD was used to determine which time points exhibited statistically significant differences between genotypes. Pearson's correlation coefficient was calculated to quantify the level of correlation between datasets, and Fisher's exact test was used to further investigate the similarities between human and mouse primary myoblasts gene expression data. All results which passed the threshold for statistical significance were tested for normal distribution using the Shapiro-Wilk normality test, all analysed data were normally distributed. A p-value of $\leq$ 5.0e-2 was considered statistically significant, and the values are reported as follows in figures: *$p \leq$ 5.0e-2, **p< 1.0e-2, ***$p <$ 1.0e-3, ****$p <$ 1.0e-4. All statistical analyses outside of differential gene expression and GO enrichment analyses were performed using GraphPad Prism 8.4.2.

A one-sided hypergeometric test with false discovery rate adjustment for multiple testing on differentially regulated reactions was used to uncover the most perturbed metabolic pathways between the two groups, as described before [139]. The flux fold change of the DMD-specific max flux and the baseline human max flux was estimated as illustrated in Equation 4.

$$flux\ fold\ change = \frac{\mathrm{MaxFlux_{DMD}+1}}{\mathrm{MaxFlux_{baseline}+1}} \qquad (4)$$

where $\mathrm{MaxFlux_{DMD}}$ is the Max Flux from DMD-specific GSMM, $\mathrm{MaxFlux_{baseline}}$ is the Max Flux from the baseline healthy human GSMM (without any constraints). To avoid 0/0 or NANs ratios, a small correction coefficient +1 was added to both DMD and healthy Max Fluxes. The log2 of flux fold change was used to identify the upregulated and downregulated metabolic reactions and pathways. To select metabolic processes characterised by statistically significant activity changes, reactions with a log2(flux fold change) greater than 1 and a log2(flux fold change) distribution above the 95th percentile were classified as "upregulated reactions", while the reactions with a log2(flux fold change) less than -0.1 and below the 5th percentile log2(flux fold change) were classified as "downregulated reactions".

Acknowledgements

The authors would like to thank S Arkle, C Crane-Robinson and K Zabłocki for the critical comments on the manuscript. SCR was partially funded through an Expanding Excellence in England (E3) grant from Research England. CA would like to acknowledge a Network Development Award from The Alan Turing Institute, grant number TNDC2-100022.

Author's contributions

MRFG, JR and LB contributed mouse experiments and transcriptomic analyses (with SCR); VM and CP contributed comparative human data; MB analysed TFBS; SV, AO and CA performed metabolic modelling and examined the metabolic pathways, LB performed immunolocalizations in spheroids; SCR and MK supervised transcriptomic analyses and DCG conceptualised the project, supervised experiments and wrote the final version of the manuscript. All authors contributed to data analysis and writing of the manuscript.

Conflicts of interest

None.

References

1. Hoffman, E. P. *et al.* Characterization of dystrophin in muscle-biopsy specimens from patients with Duchenne's or Becker's muscular dystrophy. *N. Engl. J. Med.* **318**, 1363–1368 (1988).
2. Koeks, Z. *et al.* Clinical Outcomes in Duchenne Muscular Dystrophy: A Study of 5345 Patients from the TREAT-NMD DMD Global Database. *J. Neuromuscul. Dis.* **4**, 293–306 (2017).
3. Tennyson, C. N., Klamut, H. J. & Worton, R. G. The human dystrophin gene requires 16 hours to be transcribed and is cotranscriptionally spliced. *Nat. Genet.* **9**, 184–190 (1995).
4. Shoji, E. *et al.* Early pathogenesis of Duchenne muscular dystrophy modelled in patient-derived human induced pluripotent stem cells. *Sci. Rep.* **5**, 12831 (2015).
5. Rader, E. P. *et al.* Role of dystroglycan in limiting contraction-induced injury to the sarcomeric cytoskeleton of mature skeletal muscle. *Proc. Natl. Acad. Sci. U. S. A.* (2016) doi:10.1073/pnas.1605265113.
6. Ghahramani Seno, M. M. *et al.* RNAi-mediated knockdown of dystrophin expression in adult mice does not lead to overt muscular dystrophy pathology. *Hum. Mol. Genet.* **17**, 2622–2632 (2008).

7. Waugh, T. A. *et al.* Fluoxetine prevents dystrophic changes in a zebrafish model of Duchenne muscular dystrophy. *Hum. Mol. Genet.* **23**, 4651–4662 (2014).

8. Vieira, N. M. *et al.* Jagged 1 Rescues the Duchenne Muscular Dystrophy Phenotype. *Cell* **163**, 1204–1213 (2015).

9. Dommelen, P. van, Dijk, O. van, Wilde, J. A. de & Verkerk, P. H. Early developmental milestones in Duchenne muscular dystrophy. *Dev. Med. Child Neurol.* **62**, 1198–1204 (2020).

10. Pescatori, M. *et al.* Gene expression profiling in the early phases of DMD: a constant molecular signature characterizes DMD muscle from early postnatal life throughout disease progression. *FASEB J. Off. Publ. Fed. Am. Soc. Exp. Biol.* **21**, 1210–1226 (2007).

11. Toop, J. & Emery, A. E. Muscle histology in fetuses at risk for Duchenne muscular dystrophy. *Clin. Genet.* **5**, 230–233 (1974).

12. Emery, A. E. Muscle histology and creatine kinase levels in the foetus in Duchenne muscular dystrophy. *Nature* **266**, 472–473 (1977).

13. Vassilopoulos, D. & Emery, A. E. Muscle nuclear changes in fetuses at risk for Duchenne muscular dystrophy. *J. Med. Genet.* **14**, 13–15 (1977).

14. Nguyen, F., Cherel, Y., Guigand, L., Goubault-Leroux, I. & Wyers, M. Muscle lesions associated with dystrophin deficiency in neonatal golden retriever puppies. *J. Comp. Pathol.* **126**, 100–108 (2002).

15. Bassett, D. I. *et al.* Dystrophin is required for the formation of stable muscle attachments in the zebrafish embryo. *Dev. Camb. Engl.* **130**, 5851–5860 (2003).

16. Merrick, D., Stadler, L. K. J., Larner, D. & Smith, J. Muscular dystrophy begins early in embryonic development deriving from stem cell loss and disrupted skeletal muscle formation. *Dis. Model. Mech.* **2**, 374–388 (2009).

17. Mournetas, V. *et al.* Myogenesis modelled by human pluripotent stem cells: a multi-omic study of Duchenne myopathy early onset. *J. Cachexia Sarcopenia Muscle* (2021) doi:10.1002/jcsm.12665.

18. Massouridès, E. *et al.* Dp412e: a novel human embryonic dystrophin isoform induced by BMP4 in early differentiated cells. *Skelet. Muscle* **5**, 40 (2015).

19. Tidball, J. G. Regulation of muscle growth and regeneration by the immune system. *Nat. Rev. Immunol.* **17**, 165–178 (2017).

20. Blau, H. M., Webster, C. & Pavlath, G. K. Defective myoblasts identified in Duchenne muscular dystrophy. *Proc. Natl. Acad. Sci. U. S. A.* **80**, 4856–4860 (1983).

21. Hurko, O., McKee, L., Zuurveld, J. & Swick, H. M. Comparison of Duchenne and normal myoblasts from a heterozygote. *Neurology* **37**, 675–681 (1987).

22. Yablonka-Reuveni, Z. & Anderson, J. E. Satellite cells from dystrophic (mdx) mice display accelerated differentiation in primary cultures and in isolated myofibers. *Dev. Dyn. Off. Publ. Am. Assoc. Anat.* **235**, 203–212 (2006).

23. Yeung, D. *et al.* Increased susceptibility to ATP via alteration of P2X receptor function in dystrophic mdx mouse muscle cells. *FASEB J. Off. Publ. Fed. Am. Soc. Exp. Biol.* **20**, 610–620 (2006).

24. Sacco, A. *et al.* Short telomeres and stem cell exhaustion model Duchenne muscular dystrophy in mdx/mTR mice. *Cell* **143**, 1059–1071 (2010).

25. Górecki, D. C. Dystrophin: The dead calm of a dogma. *Rare Dis. Austin Tex* **4**, e1153777 (2016).

26. Sicinski, P. *et al.* The molecular basis of muscular dystrophy in the mdx mouse: a point mutation. *Science* **244**, 1578–1580 (1989).

27. Duddy, W. *et al.* Muscular dystrophy in the mdx mouse is a severe myopathy compounded by hypotrophy, hypertrophy and hyperplasia. *Skelet. Muscle* **5**, 16 (2015).

28. DiMario, J. X., Uzman, A. & Strohman, R. C. Fiber regeneration is not persistent in dystrophic (MDX) mouse skeletal muscle. *Dev. Biol.* **148**, 314–321 (1991).

29. Massopust, R. T. *et al.* Lifetime analysis of mdx skeletal muscle reveals a progressive pathology that leads to myofiber loss. *Sci. Rep.* **10**, 17248 (2020).

30. Howard, P. L. *et al.* Dystrophin isoforms DP71 and DP427 have distinct roles in myogenic cells. *Muscle Nerve* **22**, 16–27 (1999).

31. Young, C. N. J. *et al.* Total Absence of Dystrophin Expression Exacerbates Ectopic Myofiber Calcification and Fibrosis and Alters Macrophage Infiltration Patterns. *Am. J. Pathol.* (2019) doi:10.1016/j.ajpath.2019.09.021.

32. Wertz, K. & Füchtbauer, E.-M. Dmdmdx-βgeo: A new allele for the mouse dystrophin gene. *Dev. Dyn.* **212**, 229–241 (1998).

33. Zurlo, F., Larson, K., Bogardus, C. & Ravussin, E. Skeletal muscle metabolism is a major determinant of resting energy expenditure. *J. Clin. Invest.* **86**, 1423–1427 (1990).

34. Matre, P. R. *et al.* CRISPR/Cas9-Based Dystrophin Restoration Reveals a Novel Role for Dystrophin in Bioenergetics and Stress Resistance of Muscle Progenitors. *Stem Cells Dayt. Ohio* **37**, 1615–1628 (2019).

35. Magli, A. *et al.* Time-dependent Pax3-mediated chromatin remodeling and cooperation with Six4 and Tead2 specify the skeletal myogenic lineage in developing mesoderm. *PLOS Biol.* **17**, e3000153 (2019).

36. Koo, J. H., Smiley, M. A., Lovering, R. M. & Margolis, F. L. Bex1 knock out mice show altered skeletal muscle regeneration. *Biochem. Biophys. Res. Commun.* **363**, 405–410 (2007).

37. Qin, C. Y., Cai, H., Qing, H. R., Li, L. & Zhang, H. P. Recent advances on the role of long non-coding RNA H19 in regulating mammalian muscle growth and development. *Yi Chuan Hered.* **39**, 1150–1157 (2017).

38. Sakamoto, K. *et al.* The nephroblastoma overexpressed gene (NOV/ccn3) protein associates with Notch1 extracellular domain and inhibits myoblast differentiation via Notch signaling pathway. *J. Biol. Chem.* **277**, 29399–29405 (2002).

39. Li, D. *et al.* SMYD1, the myogenic activator, is a direct target of serum response factor and myogenin. *Nucleic Acids Res.* **37**, 7059–7071 (2009).

40. Harrer, M., Lührs, H., Bustin, M., Scheer, U. & Hock, R. Dynamic interaction of HMGA1a proteins with chromatin. *J. Cell Sci.* **117**, 3459–3471 (2004).

41. Qiu, H. *et al.* Regulatory Axis of miR-195/497 and HMGA1-Id3 Governs Muscle Cell Proliferation and Differentiation. *Int. J. Biol. Sci.* **13**, 157–166 (2017).

42. Haines, B. P., Gupta, R., Jones, C. M., Summerbell, D. & Rigby, P. W. J. The NLRR gene family and mouse development: Modified differential display PCR identifies NLRR-1 as a gene expressed in early somitic myoblasts. *Dev. Biol.* **281**, 145–159 (2005).

43. Kishioka, Y. *et al.* Decorin enhances the proliferation and differentiation of myogenic cells through suppressing myostatin activity. *J. Cell. Physiol.* **215**, 856–867 (2008).

44. Mochida, Y. *et al.* Decorin modulates collagen matrix assembly and mineralization. *Matrix Biol. J. Int. Soc. Matrix Biol.* **28**, 44–52 (2009).

45. Doran, P. *et al.* Subproteomics analysis of Ca+-binding proteins demonstrates decreased calsequestrin expression in dystrophic mouse skeletal muscle. *Eur. J. Biochem.* **271**, 3943–3952 (2004).

46. ENCODE Project Consortium. The ENCODE (ENCyclopedia Of DNA Elements) Project. *Science* **306**, 636–640 (2004).

47. Vallejo-Illarramendi, A., Toral-Ojeda, I., Aldanondo, G. & López de Munain, A. Dysregulation of calcium homeostasis in muscular dystrophies. *Expert Rev. Mol. Med.* **16**, e16 (2014).

48. Farea, M., Rani, A. Q. M., Maeta, K., Nishio, H. & Matsuo, M. Dystrophin Dp71ab is monoclonally expressed in human satellite cells and enhances proliferation of myoblast cells. *Sci. Rep.* **10**, 17123 (2020).

49. Morgan, J. E. *et al.* Myogenic cell lines derived from transgenic mice carrying a thermolabile T antigen: a model system for the derivation of tissue-specific and mutation-specific cell lines. *Dev. Biol.* **162**, 486–498 (1994).

50. Kim, S. *et al.* Roles of Exosome-Like Vesicles Released from Inflammatory C2C12 Myotubes: Regulation of Myocyte Differentiation and Myokine Expression. *Cell. Physiol. Biochem. Int. J. Exp. Cell. Physiol. Biochem. Pharmacol.* **48**, 1829–1842 (2018).

51. Witkowski, J. A. & Dubowitz, V. Duchenne muscular dystrophy: studies of cell motility in vitro. *J. Cell Sci.* **76**, 225–234 (1985).

52. Melone, M. A. B., Peluso, G., Petillo, O., Galderisi, U. & Cotrufo, R. Defective growth in vitro of Duchenne muscular dystrophy myoblasts: The molecular and biochemical basis. *J. Cell. Biochem.* **76**, 118–132 (2000).

53. Nesmith, A. P. *et al.* A human in vitro model of Duchenne muscular dystrophy muscle formation and contractility. *J. Cell Biol.* **215**, 47–56 (2016).

54. Sun, C. *et al.* Duchenne muscular dystrophy hiPSC-derived myoblast drug screen identifies compounds that ameliorate disease in mdx mice. *JCI Insight* **5**, 134287 (2020).

55. Magazzù, G., Zampieri, G. & Angione, C. Multimodal regularised linear models with flux balance analysis for mechanistic integration of omics data. *Bioinforma. Oxf. Engl.* btab324 (2021) doi:10.1093/bioinformatics/btab324.

56. Durany, N., Carreras, J., Valentí, M., Cámara, J. & Carreras, J. Inactivation of phosphoglycerate mutase and creatine kinase isoenzymes in human serum. *Mol. Pathol. MP* **55**, 242–249 (2002).

57. Lagerwaard, B. *et al.* Propionate hampers differentiation and modifies histone propionylation and acetylation in skeletal muscle cells. *Mech. Ageing Dev.* **196**, 111495 (2021).

58. Capitanio, D. *et al.* Comparative proteomic analyses of Duchenne muscular dystrophy and Becker muscular dystrophy muscles: changes contributing to preserve muscle function in Becker muscular dystrophy patients. *J. Cachexia Sarcopenia Muscle* **11**, 547–563 (2020).

59. Mh, V. *et al.* Fasting increases human skeletal muscle net phenylalanine release and this is associated with decreased mTOR signaling. *PloS One* **9**, (2014).

60. Dumont, N. A. *et al.* Dystrophin expression in muscle stem cells regulates their polarity and asymmetric division. *Nat. Med.* **21**, 1455–1463 (2015).

61. Róg, J. *et al.* Dystrophic mdx mouse myoblasts exhibit elevated ATP/UTP-evoked metabotropic purinergic responses and alterations in calcium signalling. *Biochim. Biophys. Acta Mol. Basis Dis.* **1865**, 1138–1151 (2019).

62. Choi, I. Y. *et al.* Concordant but Varied Phenotypes among Duchenne Muscular Dystrophy Patient-Specific Myoblasts Derived using a Human iPSC-Based Model. *Cell Rep.* **15**, 2301–2312 (2016).

63. Onopiuk, M. *et al.* Mutation in dystrophin-encoding gene affects energy metabolism in mouse myoblasts. *Biochem. Biophys. Res. Commun.* **386**, 463–466 (2009).

64. Onopiuk, M. *et al.* Store-operated calcium entry contributes to abnormal Ca^{2+} signalling in dystrophic mdx mouse myoblasts. *Arch. Biochem. Biophys.* **569**, 1–9 (2015).

65. Dumont, N. A., Wang, Y. X. & Rudnicki, M. A. Intrinsic and extrinsic mechanisms regulating satellite cell function. *Dev. Camb. Engl.* **142**, 1572–1581 (2015).

66. Young, C. N. J. *et al.* A novel mechanism of autophagic cell death in dystrophic muscle regulated by P2RX7 receptor large-pore formation and HSP90. *Autophagy* **11**, 113–130 (2015).

67. Wang, Y. *et al.* Dystrophin is a tumor suppressor in human cancers with myogenic programs. *Nat. Genet.* **46**, 601–606 (2014).

68. Megeney, L. A. *et al.* Severe cardiomyopathy in mice lacking dystrophin and MyoD. *Proc. Natl. Acad. Sci. U. S. A.* **96**, 220–225 (1999).

69. Schuierer, M. M., Mann, C. J., Bildsoe, H., Huxley, C. & Hughes, S. M. Analyses of the differentiation potential of satellite cells from myoD-/-, mdx, and PMP22 C22 mice. *BMC Musculoskelet. Disord.* **6**, 15 (2005).

70. Zhang, H. *et al.* Human myotube formation is determined by MyoD-Myomixer/Myomaker axis. *Sci. Adv.* **6**, (2020).

71. Epstein, J. A., Lam, P., Jepeal, L., Maas, R. L. & Shapiro, D. N. Pax3 inhibits myogenic differentiation of cultured myoblast cells. *J. Biol. Chem.* **270**, 11719–11722 (1995).

72. Hildyard, J. C. W. *et al.* Single-transcript multiplex in situ hybridisation reveals unique patterns of dystrophin isoform expression in the developing mammalian embryo. *Wellcome Open Res.* **5**, 76 (2020).

73. Lidov, H. G., Byers, T. J., Watkins, S. C. & Kunkel, L. M. Localization of dystrophin to postsynaptic regions of central nervous system cortical neurons. *Nature* **348**, 725–728 (1990).

74. Kino, Y., Satoh, J. & Ishiura, S. Molecular Mechanisms of Myotonic Dystrophy: RNA-Mediated Pathogenesis and RNA-Binding Proteins. in *Myotonic Dystrophy: Disease Mechanism, Current Management and Therapeutic Development* (eds. Takahashi, M. P. & Matsumura, T.) 19–43 (Springer, 2018). doi:10.1007/978-981-13-0508-5_2.

75. Chan, L. Y., Mugler, C. F., Heinrich, S., Vallotton, P. & Weis, K. Non-invasive measurement of mRNA decay reveals translation initiation as the major determinant of mRNA stability. *eLife* **7**, e32536 (2018).

76. Sudmant, P. H. *et al.* An integrated map of structural variation in 2,504 human genomes. *Nature* **526**, 75–81 (2015).

77. Kamieniarz-Gdula, K. & Proudfoot, N. J. Transcriptional Control by Premature Termination: A Forgotten Mechanism. *Trends Genet. TIG* **35**, 553–564 (2019).

78. Chang, N. C., Chevalier, F. P. & Rudnicki, M. A. Satellite Cells in Muscular Dystrophy - Lost in Polarity. *Trends Mol. Med.* **22**, 479–496 (2016).

79. Dumont, N. A. & Rudnicki, M. A. Targeting muscle stem cell intrinsic defects to treat Duchenne muscular dystrophy. *NPJ Regen. Med.* **1**, (2016).

80. Ribeiro, A. F. *et al.* Muscle satellite cells and impaired late stage regeneration in different murine models for muscular dystrophies. *Sci. Rep.* **9**, 11842 (2019).

81. Chang, N. C. *et al.* The Dystrophin Glycoprotein Complex Regulates the Epigenetic Activation of Muscle Stem Cell Commitment. *Cell Stem Cell* **22**, 755-768.e6 (2018).

82. Brenman, J. E., Chao, D. S., Xia, H., Aldape, K. & Bredt, D. S. Nitric oxide synthase complexed with dystrophin and absent from skeletal muscle sarcolemma in Duchenne muscular dystrophy. *Cell* **82**, 743–752 (1995).

83. Colussi, C. *et al.* HDAC2 blockade by nitric oxide and histone deacetylase inhibitors reveals a common target in Duchenne muscular dystrophy treatment. *Proc. Natl. Acad. Sci. U. S. A.* **105**, 19183–19187 (2008).

84. Minetti, G. C. *et al.* Functional and morphological recovery of dystrophic muscles in mice treated with deacetylase inhibitors. *Nat. Med.* **12**, 1147–1150 (2006).

85. Tucci, V., Isles, A. R., Kelsey, G., Ferguson-Smith, A. C., & Erice Imprinting Group. Genomic Imprinting and Physiological Processes in Mammals. *Cell* **176**, 952–965 (2019).

86. Zoghbi, H. Y. & Beaudet, A. L. Epigenetics and Human Disease. *Cold Spring Harb. Perspect. Biol.* **8**, a019497 (2016).

87. Tan, X. *et al.* SmyD1, a histone methyltransferase, is required for myofibril organization and muscle contraction in zebrafish embryos. *Proc. Natl. Acad. Sci. U. S. A.* **103**, 2713–2718 (2006).

88. Tosic, M. *et al.* Lsd1 regulates skeletal muscle regeneration and directs the fate of satellite cells. *Nat. Commun.* **9**, 366 (2018).

89. Scionti, I. *et al.* LSD1 Controls Timely MyoD Expression via MyoD Core Enhancer Transcription. *Cell Rep.* **18**, 1996–2006 (2017).

90. Saccone, V. *et al.* HDAC-regulated myomiRs control BAF60 variant exchange and direct the functional phenotype of fibro-adipogenic progenitors in dystrophic muscles. *Genes Dev.* **28**, 841–857 (2014).

91. Mal, A., Sturniolo, M., Schiltz, R. L., Ghosh, M. K. & Harter, M. L. A role for histone deacetylase HDAC1 in modulating the transcriptional activity of MyoD: inhibition of the myogenic program. *EMBO J.* **20**, 1739–1753 (2001).

92. Percival, J. M. *et al.* Sildenafil reduces respiratory muscle weakness and fibrosis in the mdx mouse model of Duchenne muscular dystrophy. *J. Pathol.* **228**, 77–87 (2012).

93. Vidal, B. *et al.* Amelioration of Duchenne muscular dystrophy in mdx mice by elimination of matrix-associated fibrin-driven inflammation coupled to the αMβ2 leukocyte integrin receptor. *Hum. Mol. Genet.* **21**, 1989–2004 (2012).

94. Sinadinos, A. *et al.* P2RX7 purinoceptor: a therapeutic target for ameliorating the symptoms of duchenne muscular dystrophy. *PLoS Med.* **12**, e1001888 (2015).

95. Xie, X., Tsai, S. Y. & Tsai, M.-J. COUP-TFII regulates satellite cell function and muscular dystrophy. *J. Clin. Invest.* **126**, 3929–3941 (2016).

96. Wang, Y. X. *et al.* EGFR-Aurka Signaling Rescues Polarity and Regeneration Defects in Dystrophin-Deficient Muscle Stem Cells by Increasing Asymmetric Divisions. *Cell Stem Cell* **24**, 419-432.e6 (2019).

97. Timpani, C. A., Hayes, A. & Rybalka, E. Revisiting the dystrophin-ATP connection: How half a century of research still implicates mitochondrial dysfunction in Duchenne Muscular Dystrophy aetiology. *Med. Hypotheses* **85**, 1021–1033 (2015).

98. Kreis, R. *et al.* Brain metabolite composition in relation to cognitive function and dystrophin mutations in boys with Duchenne muscular dystrophy. *NMR Biomed.* **24**, 253–262 (2011).

99. Filippelli, R. L. & Chang, N. C. Empowering Muscle Stem Cells for the Treatment of Duchenne Muscular Dystrophy. *Cells Tissues Organs* 1–14 (2021) doi:10.1159/000514305.

100. Nsiah-Sefaa, A. & McKenzie, M. Combined defects in oxidative phosphorylation and fatty acid β-oxidation in mitochondrial disease. *Biosci. Rep.* **36**, e00313 (2016).

101. Bradley, W. G. *Neurology in Clinical Practice*. (Taylor & Francis, 2004).

102. Scholte, H. R. & Busch, H. F. Early changes of muscle mitochondria in Duchenne dystrophy. Partition and activity of mitochondrial enzymes in fractionated muscle of unaffected boys and adults and patients. *J. Neurol. Sci.* **45**, 217–234 (1980).

103. Kelly-Worden, M. & Thomas, E. Mitochondrial Dysfunction in Duchenne Muscular Dystrophy. *Open J. Endocr. Metab. Dis.* **4**, 211–218 (2014).

104. Korotkova, M. & Lundberg, I. E. The skeletal muscle arachidonic acid cascade in health and inflammatory disease. *Nat. Rev. Rheumatol.* **10**, 295–303 (2014).

105. Lee-Young, R. S. *et al.* Glucose-6-phosphate dehydrogenase contributes to the regulation of glucose uptake in skeletal muscle. *Mol. Metab.* **5**, 1083–1091 (2016).

106. Fulco, M. *et al.* Glucose restriction inhibits skeletal myoblast differentiation by activating SIRT1 through AMPK-mediated regulation of Nampt. *Dev. Cell* **14**, 661–673 (2008).

107. Rodrigues, M. & Yokota, T. An Overview of Recent Advances and Clinical Applications of Exon Skipping and Splice Modulation for Muscular Dystrophy and Various Genetic Diseases. *Methods Mol. Biol. Clifton NJ* **1828**, 31–55 (2018).

108. Vila, M. C. *et al.* Morpholino-induced exon skipping stimulates cell-mediated and humoral responses to dystrophin in mdx mice. *J. Pathol.* **248**, 339–351 (2019).

109. Sharma, D. *et al.* Co-delivery of indoleamine 2,3-dioxygenase prevents loss of expression of an antigenic transgene in dystrophic mouse muscles. *Gene Ther.* **24**, 113–119 (2017).

110. Mangeot, P. E. *et al.* Genome editing in primary cells and in vivo using viral-derived Nanoblades loaded with Cas9-sgRNA ribonucleoproteins. *Nat. Commun.* **10**, 45 (2019).

111. Petkov, P. M. *et al.* An efficient SNP system for mouse genome scanning and elucidating strain relationships. *Genome Res.* **14**, 1806–1811 (2004).

112. McGreevy, J. W., Hakim, C. H., McIntosh, M. A. & Duan, D. Animal models of Duchenne muscular dystrophy: from basic mechanisms to gene therapy. *Dis. Model. Mech.* **8**, 195–213 (2015).

113. Augusto, V., Padovani, C., Eduardo, G. & Campos, R. Skeletal muscle fiber types in C57BL6J mice. *J Morphol Sci* **21**, 89–94 (2004).

114. S. Andrews. FastQC: A Quality Control Tool for High Throughput Sequence Data. (2010).

115. F. Krueger. Trim Galore! A Quality Trimming Tool for High Throughput Sequence Data. (2012).

116. Dobin, A. *et al.* STAR: ultrafast universal RNA-seq aligner. *Bioinforma. Oxf. Engl.* **29**, 15–21 (2013).

117. Li, H. *et al.* The Sequence Alignment/Map format and SAMtools. *Bioinforma. Oxf. Engl.* **25**, 2078–2079 (2009).

118. Love, M. I., Huber, W. & Anders, S. Moderated estimation of fold change and dispersion for RNA-seq data with DESeq2. *Genome Biol.* **15**, 550 (2014).

119. R Core Team. R: A Language and Environment for Statistical Computing. *R Found. Stat. Comput. Vienna Austria* (2017).

120. Lawrence, M. *et al.* Software for computing and annotating genomic ranges. *PLoS Comput. Biol.* **9**, e1003118 (2013).

121. Benjamini, Y. & Hochberg, Y. Controlling the False Discovery Rate: A Practical and Powerful Approach to Multiple Testing. *J. R. Stat. Soc. Ser. B Methodol.* **57**, 289–300 (1995).

122. Yu, G., Wang, L.-G., Han, Y. & He, Q.-Y. clusterProfiler: an R package for comparing biological themes among gene clusters. *Omics J. Integr. Biol.* **16**, 284–287 (2012).

123. Supek, F., Bošnjak, M., Škunca, N. & Šmuc, T. REVIGO Summarizes and Visualizes Long Lists of Gene Ontology Terms. *PLOS ONE* **6**, e21800 (2011).

124. Szklarczyk, D. *et al.* STRING v11: protein-protein association networks with increased coverage, supporting functional discovery in genome-wide experimental datasets. *Nucleic Acids Res.* **47**, D607–D613 (2019).

125. Piechota, M., Korostynski, M., Ficek, J., Tomski, A. & Przewlocki, R. Seqinspector: position-based navigation through the ChIP-seq data landscape to identify gene expression regulators. *BMC Bioinformatics* **17**, 85 (2016).

126. Robinson, J. L. *et al.* An atlas of human metabolism. *Sci. Signal.* **13**, eaaz1482 (2020).

127. Aoyagi, T. *et al.* Two different modes of enzymatic changes in serum with progression of Duchenne muscular dystrophy. *Clin. Chim. Acta Int. J. Clin. Chem.* **129**, 165–173 (1983).

128. Sánchez, B. J. *et al.* Improving the phenotype predictions of a yeast genome-scale metabolic model by incorporating enzymatic constraints. *Mol. Syst. Biol.* **13**, 935 (2017).

129. Angione, C. Integrating splice-isoform expression into genome-scale models characterizes breast cancer metabolism. *Bioinforma. Oxf. Engl.* **34**, 494–501 (2018).

130. Rawls, K. D. *et al.* A simplified metabolic network reconstruction to promote understanding and development of flux balance analysis tools. *Comput. Biol. Med.* **105**, 64–71 (2019).

131. Zampieri, G., Vijayakumar, S., Yaneske, E. & Angione, C. Machine and deep learning meet genome-scale metabolic modeling. *PLoS Comput. Biol.* **15**, e1007084 (2019).

132. Heirendt, L. *et al.* Creation and analysis of biochemical constraint-based models using the COBRA Toolbox v.3.0. *Nat. Protoc.* **14**, 639–702 (2019).

133. Chiron, S. *et al.* Complex interactions between human myoblasts and the surrounding 3D fibrin-based matrix. *PloS One* **7**, e36173 (2012).

134. Corona, B. T. *et al.* Further development of a tissue engineered muscle repair construct in vitro for enhanced functional recovery following implantation in vivo in a murine model of volumetric muscle loss injury. *Tissue Eng. Part A* **18**, 1213–1228 (2012).

135. Mei, C. *et al.* Three-dimensional spherical gelatin bubble-based scaffold improves the myotube formation of H9c2 myoblasts. *Biotechnol. Bioeng.* **116**, 1190–1200 (2019).

136. Kim, W. *et al.* Efficient myotube formation in 3D bioprinted tissue construct by biochemical and topographical cues. *Biomaterials* **230**, 119632 (2020).

137. Chen, B., You, W., Wang, Y. & Shan, T. The regulatory role of Myomaker and Myomixer-Myomerger-Minion in muscle development and regeneration. *Cell. Mol. Life Sci. CMLS* **77**, 1551–1569 (2020).

138. Stern-Straeter, J. *et al.* Characterization of human myoblast differentiation for tissue-engineering purposes by quantitative gene expression analysis. *J. Tissue Eng. Regen. Med.* **5**, e197–e206 (2011).

139. Yaneske, E., Zampieri, G., Bertoldi, L., Benvenuto, G. & Angione, C. Genome-scale metabolic modelling of SARS-CoV-2 in cancer cells reveals an increased shift to glycolytic energy production. *FEBS Lett.* **595**, 2350–2365 (2021).

140. Rapaport, D., Fuchs, O., Nudel, U. & Yaffe, D. Expression of the Duchenne muscular dystrophy gene products in embryonic stem cells and their differentiated derivatives. *J. Biol. Chem.* **267**, 21289–21292 (1992).

141. Gonzalez, J. P. *et al.* Small Fractions of Muscular Dystrophy Embryonic Stem Cells Yield Severe Cardiac and Skeletal Muscle Defects in Adult Mouse Chimeras. *Stem Cells Dayt. Ohio* **35**, 597–610 (2017).

142. Young, C. N. J. *et al.* P2X7 purinoceptor alterations in dystrophic mdx mouse muscles: relationship to pathology and potential target for treatment. *J. Cell. Mol. Med.* **16**, 1026–1037 (2012).

143. Young, C. N. J. *et al.* Sustained activation of P2X7 induces MMP-2-evoked cleavage and functional purinoceptor inhibition. *J. Mol. Cell Biol.* **10**, 229–242 (2018).

144. Howard, Z. M. *et al.* Early Inflammation in Muscular Dystrophy Differs between Limb and Respiratory Muscles and Increases with Dystrophic Severity. *Am. J. Pathol.* **191**, 730–747 (2021).

145. Al-Khalidi, R. *et al.* Zidovudine ameliorates pathology in the mouse model of Duchenne muscular dystrophy via P2RX7 purinoceptor antagonism. *Acta Neuropathol. Commun.* **6**, (2018).

146. Otto, T. *et al.* Cell cycle-targeting microRNAs promote differentiation by enforcing cell-cycle exit. *Proc. Natl. Acad. Sci.* (2017) doi:10.1073/pnas.1702914114.

Figure Legends

Figure 1: **Differential gene expression between *Dmd*^{mdx} and WT mouse primary myoblasts**

a) Sample-based hierarchical clustering heatmap based on the top 500 genes with the highest standard deviation for *Dmd*^{mdx} vs. WT based on RNA-Seq data. Colour represents dissimilarity between samples, based on the Euclidean distance, from dark blue (0) for identical samples to white (40) for the most distinct.

b) Volcano plot for $\mathit{Dmd}^{\mathrm{mdx}}$ versus WT primary mouse myoblast differential gene expression analysis. Circles represent individual genes, with colour representing significance and direction of dysregulation (blue-significantly downregulated; red-significantly upregulated; black-not significantly dysregulated). Circle position represents fold change on a log2 scale for the x-axis and adjusted *p*-value on a -log10 scale for the y-axis. Horizontal dotted line represents the threshold of an adjusted *p*-value of 5.0e-25.0e-2 or lower while the vertical doted lines represent the threshold for the absolute log2 fold change of 1.

c) Clustered heatmap of genes of interest from the dysregulated gene list of $\mathit{Dmd}^{\mathrm{mdx}}$ vs. WT primary myoblasts. Colour represents the z-score such that each gene has a mean of 0 and standard deviation of 1 to allow direct comparisons.

Figure 2: **Correlation of significantly dysregulated gene expressions between $\mathit{Dmd}^{\mathrm{mdx}}$ and $\mathit{Dmd}^{\mathrm{mdx\text{-}\beta geo}}$ vs. WT.**

a) Sample-based hierarchical clustering heatmap based on the top 500 genes with the highest standard deviation for $\mathit{Dmd}^{\mathrm{mdx\text{-}\beta geo}}$ vs. $\mathit{Dmd}^{\mathrm{mdx}}$ Colour represents dissimilarity between samples based on the Euclidean distance, from dark blue (0) for identical samples to white (40) for the most distinct. Note the absence of sample segregation into two groups corresponding to genotypes.

b) Volcano plot for $\mathit{Dmd}^{\mathrm{mdx\text{-}\beta geo}}$ vs. $\mathit{Dmd}^{\mathrm{mdx}}$ primary mouse myoblast differential gene expression analysis. Circles represent individual genes, with colour representing significance and direction of dysregulation (blue-significantly downregulated; red-significantly upregulated; black-not significantly dysregulated). Circle position represents fold change on a log2 scale for the x-axis and adjusted *p*-value on a -log10 scale for the y-axis. Horizontal dotted line represents the threshold of an adjusted *p*-value of 5.0e-2 or lower while the vertical doted lines represent the threshold for the absolute log2 fold change of 1.

c) log2 fold change values ($\mathit{Dmd}^{\mathrm{mdx}}$ versus WT on the x-axis and $\mathit{Dmd}^{\mathrm{mdx\text{-}\beta geo}}$ versus WT on the y-axis) for genes significantly dysregulated in one or both dystrophic primary mouse myoblasts vs. WT. Pearson's correlation coefficients (r) and *p*-value are shown. Green circles represent genes significantly dysregulated in $\mathit{Dmd}^{\mathrm{mdx\text{-}\beta geo}}$ vs. WT, blue circles represent genes significantly dysregulated in $\mathit{Dmd}^{\mathrm{mdx}}$ vs. WT and red circles represent gernes significantly dysregulated in both.

Figure 3: **Overrepresentation of TF binding sites in genes downregulated in *Dmd*^{mdx} myoblasts.**

Averaged ChIP-Seq signal histograms for each of the significantly overrepresented TFBS in downregulated genes. Histograms are centred around the transcription start site (TSS) of each gene. x-axis – distance upstream and downstream from the TSS of each gene, y-axis - ChIP-Seq signal for each location averaged for all gene promoters in the submitted list; red line - downregulated genes, blue line - upregulated genes, green line - reference signal (based on 1000 random gene promoters); Bonferroni-corrected p-value of TF signal overrepresentation vs reference: *** < 1.0e-3; ** < 1.0e-2.

a) MYOD (adjusted p-value: $2.9e^{-21}$, track GEO accession GSM915165), b) TCF12 ($1e^{-19}$, GSM915178), c) MYOG ($5.6e^{-19}$, GSM915164); d) TCF3 (0.0033, GSM915177); e) Heatmap of normalised TF-binding signal for each of the TFs overrepresented in genes downregulated in *Dmd*^{mdx} myoblasts. Genes that did not show significant binding above background (as provided by the seqinspector tool) were assigned TF binding signal of 0.

Figure 4: **Results of GO category enrichment analysis for biological processes on significantly downregulated gene lists from *Dmd*^{mdx} and *Dmd*$^{mdx\text{-}\beta geo}$ versus WT differential gene expression analyses.**

a) Bubble plot of the overlapping GO categories enriched in *Dmd*^{mdx} and *Dmd*$^{mdx\text{-}\beta geo}$ versus WT downregulated genes lists. Bubble size represents the number of genes from the downregulated gene lists belonging to the GO category and the bubble colour depicts the adjusted *p*-value from red (0) to blue (8.0e-3). **b**) Bubble plot of GO categories enriched in *Dmd*^{mdx} versus WT downregulated genes lists following REVIGO redundancy filtering (See methods). Bubble size represents the number of genes from the downregulated gene lists belonging to the GO category and the bubble colour depicts the adjusted *p*-value from red (0) to blue (1.0e-2).

Figure 5: **Dystrophic primary myoblasts show functional abnormalities.**

a) Proliferation analysis in myoblasts from *Dmd*^{mdx}, *Dmd*$^{mdx\text{-}\beta geo}$, C57BL/10 and C57BL/6 mice using a BrdU incorporation assay. (Left) Representative examples of BrdU flow cytometric dot plots from C57BL/10 and *Dmd*^{mdx} cells after 6 hours of incorporation, with FL-1 channel corresponding to BrdU fluorescence intensity and FSC channel denoting the cell size. (Right) Graph showing significantly increased proliferation of dystrophic myoblasts presented as ratio of BrdU-positive dystrophic cells relative to the respective wild type controls. Errors bars represent mean ± SEM, n = 3 or 4, * = $p \leq$ 5.0e-2, ** = $p <$ 1.0e-2 (Student's unpaired t-test). **b**) Cell chemotaxis analysis in myoblasts from

Dmd$^{\mathrm{mdx}}$, *Dmd*$^{\mathrm{mdx\text{-}\beta geo}}$, and respective wild type controls. Cells were seeded on a trans-well insert and allowed to penetrate towards the bottom well containing either proliferation medium or serum-free medium complemented with cytokines. Graph shows significantly reduced chemotaxis of dystrophic myoblasts represented as the relative number of cells present on the well-side of the membrane after 12 hours. Error bars represent mean ± SEM, n = 3 or 4, * = $p < 5.0\text{e-}2$, ** = $p < 1.0\text{e-}2$ and *** = $p < 1.0\text{e-}3$ (Student's unpaired t-test). **c**) Altered expression of differentiation markers in *Dmd*$^{\mathrm{mdx}}$ compared to C57BL/10 myoblasts. Results of qPCR expression analyses of *Myh1, Myog and Mymk* markers at specific timepoints over the 6-day period of spheroid differentiation. Individual values for biological replicates normalised to *Gapdh* expression and relative to wild type values at the commencement of differentiation (t=0) are shown. Error bars represent mean ± SEM, n = 3, * = $p \leq 5.0\text{e-}2$, ** = $p < 1.0\text{e-}2$ and **** = $p < 1.0\text{e-}4$ (two-way ANOVA was used to determine the statistical significance between groups and time-points over the 6-day period and Fisher's LSD was used to determine which timepoints exhibited a significant difference between groups).

Figure 6: **Correlation of significantly dysregulated gene expressions between mouse dystrophic and WT myoblast cell lines (SC5 vs.IMO) and of significantly enriched GO categories in the downregulated gene list for primary *Dmd*$^{\mathrm{mdx}}$ myoblasts and corresponding cell lines.**

a) Sample-based hierarchical clustering heatmap, colour represents dissimilarity between samples based on the Euclidean distance, from black for identical samples to white for more distinct samples.

b) Volcano plot, showing the results of differential expression analysis between SC5 and IMO. Circles represent individual genes, with their colour representing significance and direction of dysregulation (blue-significantly downregulated; red-significantly upregulated; black-not significantly dysregulated). Circle position represents fold change on a log2 scale for the x-axis and adjusted *p*-value on a -log10 scale for the y-axis. Horizontal dotted line represents the threshold of an adjusted *p*-value of 5.0e-2 while the vertical doted lines represent the threshold for the absolute log2 fold change of 1.

c) Venn diagrams representing the overlap between genes dysregulated in SC5 and primary *Dmd*$^{\mathrm{mdx}}$ myoblasts vs. WT as well as the overlap between GO categories for biological processes overrepresented in both downregulated gene lists. Number in the white circle enumerates dysregulated genes or enriched GO categories in SC5 vs. IMO, black circle those of *Dmd*$^{\mathrm{mdx}}$ vs. WT and grey area numbers represent overlap between these two sets. d) Bubble plot of the overlapping GO categories following redundancy filtering applied to the 61 categories identified (panel c). Bubble size represents the number of genes from the downregulated gene lists belonging to the category and bubble colour represents the adjusted *p*-value from red (0) to blue (1.0e-2).

Figure 7: **Correlation of significantly dysregulated gene expressions between human and mouse dystrophic and WT primary myoblasts and of the corresponding significantly enriched GO categories in the downregulated gene list for the human and Dmd^{mdx} myoblast data.**

a) Sample-based hierarchical clustering heatmap, represented as described before.

b) Volcano plot, showing the results of differential expression analysis between DMD and healthy myoblasts. Circles represent individual genes, with their colour representing significance and direction of dysregulation (blue-significantly downregulated; red-significantly upregulated; black-not significantly dysregulated). Circle position represents fold change on a log2 scale for the x-axis and adjusted *p*-value on a -log10 scale for the y-axis. Horizontal dotted line represents the threshold of an adjusted *p*-value of 5.0e-2 while the vertical doted lines represent the threshold for the absolute log2 fold change of 1.

c) log2 fold change values (*Dmd*^{mdx} versus WT on the x-axis and human DMD versus WT on the y-axis) for genes significantly dysregulated in one or both dystrophic vs. WT primary myoblasts. Pearson's correlation coefficients (r) and *p*-values are shown. Green circles represent genes significantly dysregulated in DMD, blue circles represent genes significantly dysregulated in *Dmd*^{mdx} vs. WT and red circles represent genes significantly dysregulated in both. The number of genes found in each quadrant is shown.

d) Venn diagrams representing the overlap between genes dysregulated in primary human DMD and *Dmd*^{mdx} myoblasts vs. WT as well as the overlap between GO categories for biological processes overrepresented in both downregulated gene lists. Number in the white circle enumerates dysregulated genes or enriched GO categories in human DMD vs. healthy, black circle those of *Dmd*^{mdx} vs. WT and grey area numbers represent overlaps between these two sets.

e) Bubble plot of the overlapping GO categories following redundancy filtering applied to the 61 categories identified (panel d). Bubble size represents the number of genes from the downregulated gene lists belonging to the GO category and the bubble colour depicts the adjusted *p*-value from red (0) to blue (7.0e-3).

Figure 8: **Correlation of enriched GO categories between primary *Dmd*^{mdx} mouse myoblasts, *Dmd*^{mdx} mouse myoblast cell line, and human primary DMD myoblasts.**

a) Venn diagram representing the overlap between GO categories for biological processes overrepresented in downregulated gene lists in primary human DMD, *Dmd*^{mdx} myoblasts and established *Dmd*^{mdx} myoblast cell line (SC5). Numbers in each area enumerate enriched GO categories in individual datasets and those overlapping (see the graphic legend).

b) Bubble plot of the overlapping GO categories following redundancy filtering applied to the 49 categories identified (panel a). Bubble size represents the number of genes from the downregulated gene lists belonging to the given GO category and bubble colour depicts the adjusted *p*-value from red (0) to blue (8.0e-3).

Figure 9: ***Metabolic pathway alterations in DMD primary myoblasts***

The differential log2FC of DMD-specific metabolic model was compared with respect to the healthy Human metabolic model. (a) Heatmap representing the differential metabolic activity of the pathways and proteins. (Left) Differential flux change of metabolic pathways. (Right) Flux fold change of the activity of enzymes, represented by proteins. (b) Visualisation of the alteration in the reactions in metabolic pathways. The red colour represents the upregulated or overactive metabolic pathways, and the blue colour represents the downregulated or underactive metabolic pathways. The full names of the reactions presented in Figure 10 are provided in Table S12

Figure 10: **Natural history of DMD.**

⍰ Embryonic stem cells (ES) express dystrophin Dp71 [140] but its loss is not linked with arrested development. Yet, minor admixture of ES lacking Dp427 results in severe dystrophy [141]: **Defects in myogenic stem cells** (SC) descendant from DMD ES must be responsible, because in myofibre syncytium, lack of dystrophin caused by small proportion of DMD nuclei would be compensated and damage prevented. Early mesoderm committed human cells express Dp412e [18] and ⍰ DMD manifests before entry into the skeletal muscle compartment [17]. ⍰ DMD abnormalities are found in dystrophic human [11–13], dog [14], zebrafish [15] and mouse embryos, with stem cell dysfunctions (hyperproliferation and death), disrupted myotube formation [16] and fibrosis as intrinsic features in developing muscle [17]. Typical dystrophic abnormalities (e.g., high serum CK) occur in new-borns years before diagnosis [9,10].

In **adult muscle**, healthy myogenic cells, myotubes and myofibres express Dp427 and DAPC assembles in differentiating fibres, supporting their functions. Impaired muscle regeneration occurs due to: ⍰ Cell-autonomous defects in dystrophic satellite cells (SC) affecting asymmetric cell divisions

[24,60,65], hyperproliferation of dystrophic myoblasts (this work) and purinergic hypersensitivity [25,142], anomalous migration of DMD myoblasts: reduced under physiological conditions (this work) but augmented in the inflammatory environment [143] and accelerated dystrophic myoblast differentiation (this work and Yablonka-Reuveni and Anderson, 2006) with defects in differentiating myotubes lacking Dp427 [4]. Resulting mature muscle lacking DAPC show contraction-induced injury but dystrophin ablation in fully differentiated myofibres does not trigger muscular dystrophy [5,6]. Chronic inflammation exacerbates muscle damage [94,144,145], but specific inflammatory mediators are also needed for regeneration [19]. Muscle fibrosis intensifies, as the progressing loss of regenerative potential results in myofibres being replaced by the connective tissue.

Figure S1: **Differential expression of muscle programme markers in primary myoblasts from *Dmd*^{mdx} and *Dmd*$^{mdx\text{-}\beta geo}$ mice.**

Results of qPCR expression analyses of indicated markers relative to wild type, normalized to *Gapdh,* shown as individual datapoints for biological replicates. Error bars represent mean ± SEM, n = 3, * = p < 5.0e-2, ** = p ≤ 1.0e-2, *** = p ≤ 1.0e-3, **** = p ≤ 1.0e-4 (Student's unpaired t-test).

Figure S2: **Immunodetection of the sarcomeric myosin heavy chain 4 in *Dmd*^{mdx} and BL/10 in differentiated spheroids.**

Representative immunofluorescence micrographs of sections across spheroids differentiated for 7 days showing presence of MYH4 protein (green). Cell nuclei stained with DAPI (blue). Scale bar = 50µm).

Figure S3: **Decreased cell chemotaxis of dystrophic established mouse myoblasts.**

In the trans-well assay, cells were migrating towards the well containing proliferation medium. Graph shows relative values of individual replicates revealing significantly reduced movement of dystrophic cells compared to their WT equivalent. Error bars represent mean ± SEM, n = 4, ** = p < 1.0e-2 (Student's unpaired t-test).

Figure S4: **Immunodetection of Dp427 in WT primary mouse myoblasts.**

Representative immunofluorescence micrographs of sections across C57BL/10 *tibialis anterior* muscle and primary *Dmd*^{mdx} myoblasts stained with an antibody detecting epitopes in exons 31/32 of Dp427. Note the expected immunofluorescence signal (green) under the sarcolemma of myofibers and absence of any discernible dystrophin immunoreactivity in myoblasts in culture, reacted and imaged under conditions identical to those used for muscle sections. Negative (no primary antibody) control shown. l indicates the specificity of the staining. Cell nuclei stained with DAPI (blue). Scale bar = 50 µm.

Figure S5: **STRING interaction diagram of genes in the GO category: Negative regulation of gene expression, epigenetic.**

Interaction network representing genes in GO:0045814. Each node depicts a gene; edges between nodes indicate interactions between protein products of the corresponding genes and the aggregated interaction scores from experimental data and interaction databases (see the Edge Confidence graphic legend for details). Genes significantly downregulated in dystrophic myoblasts are highlighted in red and the common interactor between all significantly downregulated genes (Kdma1) is highlighted in yellow. Isolated nodes are not shown.

Figure S6: **Decreased expression of Dp71 transcript in primary myoblasts from *Dmd*^{mdx} mice.**

Results of qPCR expression assay shown as normalised individual datapoints for biological replicates relative to wild type, normalised to *Gapdh*. Error bars represent mean ± SEM, n = 3, * = p<5.0e-2 (Student's unpaired t-test).

Figure S7: **Differential metabolic pathway and reaction analysis.**

Visualisation of the alteration in the reactions in pyruvate metabolism, glycolysis/gluconeogenesis metabolic pathway and glycosphingolipid biosynthesis-lacto and neolacto series pathway, transport reactions and enzyme activities. The red colour represents the upregulated or overactive metabolic pathways, and blue the downregulated or underactive ones. The full name of the reactions presented in Figure S7 are provided in Table S12.

Figure S8: **The purity of myoblasts isolated from the *gastrocnemius* muscle.**

(a) Example MyoD staining (red signal) and Hoechst nuclear labelling (blue) in primary myoblast cultures isolated from mdx and wild-type gastrocnemii. Representative immunofluorescent image from three tiles are presented and the negative control (no primary antibody) is also shown. (Size bar = 20 μm). (b) Graph showing percentage of cells positive for MyoD from the total number of cells identified by the nuclei labelling with Hoechst enumerated using the counter cells function in the ImageJ software. The purity of wt and mdx myoblast cultures was between 93% and 100%. Error bars represent the mean number of cells with SD for three tile images and the difference is not statistically significant.

Table legends

Table S1: **Genes significantly dysregulated in *Dmd*$^{\mathrm{mdx}}$ vs. WT primary myoblasts.**

From left to right, columns show ENSEMBL gene id, gene symbol, log2 fold change between *Dmd*$^{\mathrm{mdx}}$ and WT primary myoblasts, adjusted *p*-value as output by DESeq2, average FPKM for *Dmd*$^{\mathrm{mdx}}$ and WT groups. Genes are ordered from most downregulated to most upregulated.

Table S2: **Tabulation of genes significantly dysregulated in *Dmd*$^{\mathrm{mdx\text{-}\beta geo}}$ vs. WT primary myoblasts.**

From left to right, columns show ENSEMBL gene id, gene symbol, log2 fold change between *Dmd*$^{\mathrm{mdx\text{-}\beta geo}}$ and WT primary myoblasts, adjusted *p*-value as output by DESeq2, average FPKM for *Dmd*$^{\mathrm{mdx\text{-}\beta geo}}$ and WT groups. Genes are ordered from most downregulated to most upregulated.

Table S3: **Identification of putative molecular regulators of genes altered in Dmd$^{\mathrm{mdx}}$ myoblasts.**

The overrepresentation of binding sites for transcriptional regulators in the promoter region of the altered transcripts was identified using the seqinspector online resource (see Materials and Methods).

A) TFBS analysis results for transcripts upregulated in *Dmd*$^{\mathrm{mdx}}$ myoblasts. Column legend: id - ChIP-Seq track id; name - TF name, followed by the index of ChIP-Seq track for this TF; p-value - t-test p-value for overrepresentation of ChIP-Seq signal; Bonferroni - Bonferroni-corrected p-value; foldchange - a ratio of ChIP-Seq signal averaged across all promoters in the gene list versus 1000 random gene promoters; backgroundmean - averaged signal from the track across 1000 random gene promoters; querymean - averaged signal across all promoters from the submitted list. B. TFBS analysis results for transcripts downregulated in Dmd$^{\mathrm{mdx}}$ myoblasts. columns - as in A. **C**) top 10 genes for each of the significantly overrepresented TFs for transcripts downregulated in Dmd$^{\mathrm{mdx}}$. **D-**

G) TFBS analysis results (column legend as in A) for the following gene lists: upregulated in Dmd$^{mdx\text{-}\beta geo}$; downregulated in Dmd$^{mdx\text{-}\beta geo}$; upregulated in SC-5; downregulated in SC-5. **H**) gene lists as submitted to the seqinspector tool, including gene symbols that were translated for database compatibility.

Table S4: **GO categories significantly enriched in the downregulated gene lists from primary Dmd^{mdx} vs. WT and $Dmd^{md\text{-}\beta geo}$ vs. WT.**

Columns A and D show the GO category ID, columns B and E show GO category description and columns C and F show adjusted *p*-value for GO categories enriched in the significantly downregulated genes in primary *Dmd*^{mdx} and *Dmd*$^{mdx\text{-}\beta geo}$ myoblasts, respectively. GO categories are ordered from the lowest (top) to the highest (bottom) *p*-value for each analysis and GO categories significantly enriched in both analyses are highlighted in red.

Table S5: **Genes significantly dysregulated in SC5 (dystrophic) vs. IMO (WT) myoblast cell line.**

From left to right, columns show ENSEMBL gene id, gene symbol, log2 fold change between SC5 and IMO primary myoblasts, adjusted *p*-value as outputted by DESeq2, average FPKM for SC5 and IMO groups. Genes are ordered from most downregulated to most upregulated.

Table S6: **GO categories significantly enriched in the downregulated gene lists from primary *Dmd*^{mdx} vs. WT and SC5 vs. IMO cell lines.**

Columns A and D show the GO category ID, columns B and E show GO description and columns C and F show adjusted *p*-value for GO categories enriched in the significantly downregulated genes in SC5 myoblast cell line and primary *Dmd*^{mdx} myoblasts, respectively. GO categories are ordered from the lowest (top) to the highest (bottom) *p*-value for each analysis and GO categories significantly enriched in both analyses are highlighted in red.

Table S7: **Genes significantly dysregulated in DMD vs. healthy primary human myoblasts.**

From left to right, columns show ENSEMBL gene id, gene symbol, log2 fold change between DMD and healthy human primary myoblasts, adjusted *p*-value as outputted by DESeq2, average FPKM for human DMD and health groups. Genes are ordered from most downregulated to most upregulated.

Table S8: **GO categories significantly enriched in the downregulated gene lists from dystrophic vs. WT human primary myoblasts and *Dmd*^{mdx} vs. WT mouse primary myoblasts.**

Columns A and D show GO category ID, columns B and E show GO category description and columns C and F show adjusted *p*-values for GO categories enriched in the significantly downregulated genes in primary human DMD and mouse *Dmd*^{mdx} myoblasts, respectively. GO categories are ordered from the lowest (top) to the highest (bottom) *p*-value for each analysis and GO categories significantly enriched in both analyses are highlighted in red.

Table S9: **Interactions between genes in the GO category GO:0045814: "Negative regulation of gene expression, epigenetic" generated in STRING.**

Columns A and B show nodes connected by an edge, column C shows the interaction score if one has been determined experimentally, column D shows the interaction score if an interaction is present in a database feeding into STRING and column E shows the combined interaction score.

Table S10: **Primers used in real-time quantitative PCR analysis.**

Primers were designed specifically except *Gapdh* primer set, which was taken from [146].

Table S11: **Transcriptomic and enzyme-constrained flux rate of metabolic pathways and processes, and enrichment analysis results.**

Table S12: **Full name of reactions presented in the metabolic map views (Figure 10, S7).**

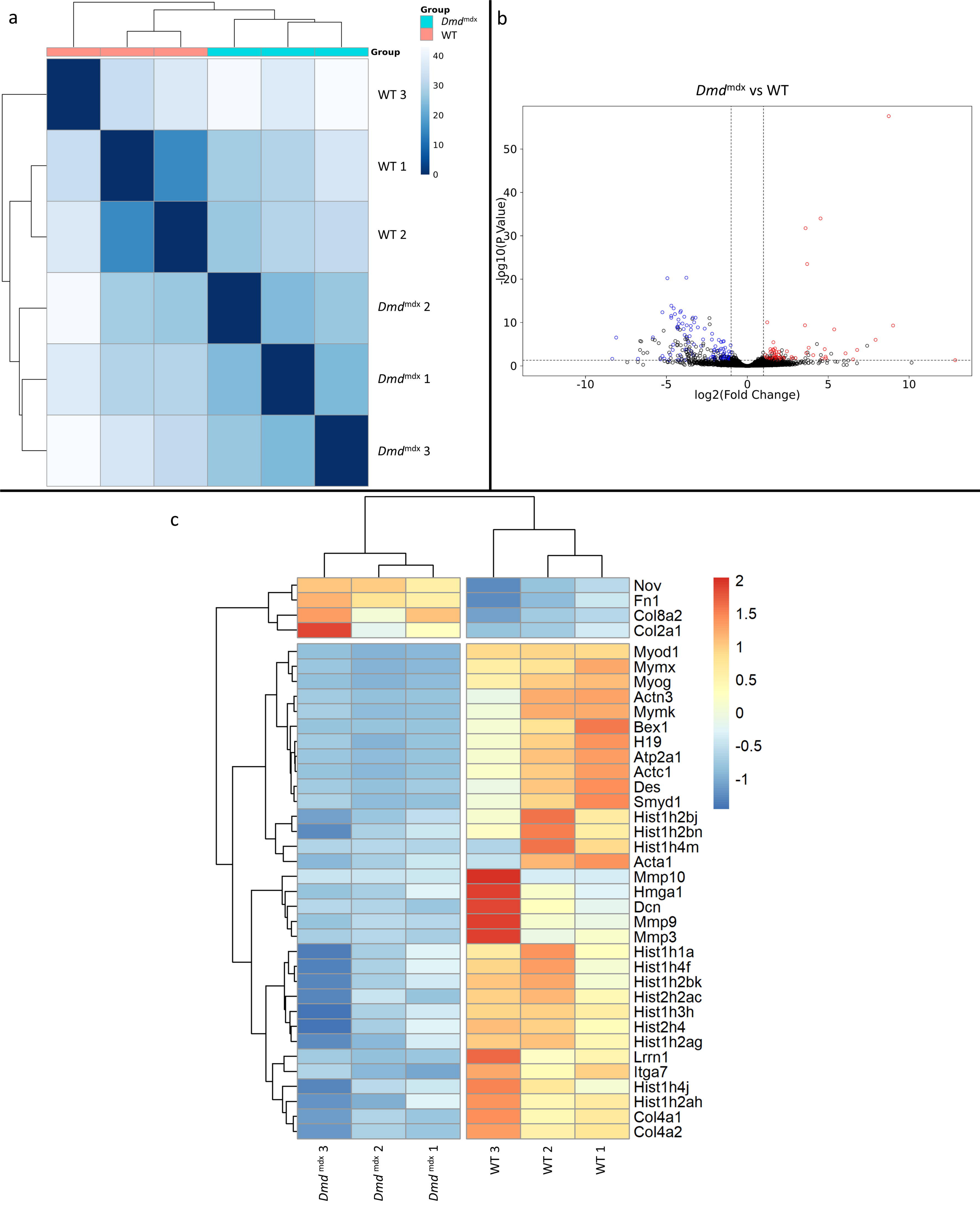
a
Group
Dmd^mdx
WT
Group
40
30
20
10
0
WT 3
WT 1
WT 2
Dmd^mdx 2
Dmd^mdx 1
Dmd^mdx 3
b
Dmd^mdx vs WT
-log10(P Value)
50
40
30
20
10
0
-10
-5
0
5
10
log2(Fold Change)
c
Nov
Fn1
Col8a2
Col2a1
Myod1
Mymx
Myog
Actn3
Mymk
Bex1
H19
Atp2a1
Actc1
Des
Smyd1
Hist1h2bj
Hist1h2bn
Hist1h4m
Acta1
Mmp10
Hmga1
Dcn
Mmp9
Mmp3
Hist1h1a
Hist1h4f
Hist1h2bk
Hist2h2ac
Hist1h3h
Hist2h4
Hist1h2ag
Lrrn1
Itga7
Hist1h4j
Hist1h2ah
Col4a1
Col4a2
2
1.5
1
0.5
0
-0.5
-1
Dmd mdx 3
Dmd mdx 2
Dmd mdx 1
WT 3
WT 2
WT 1

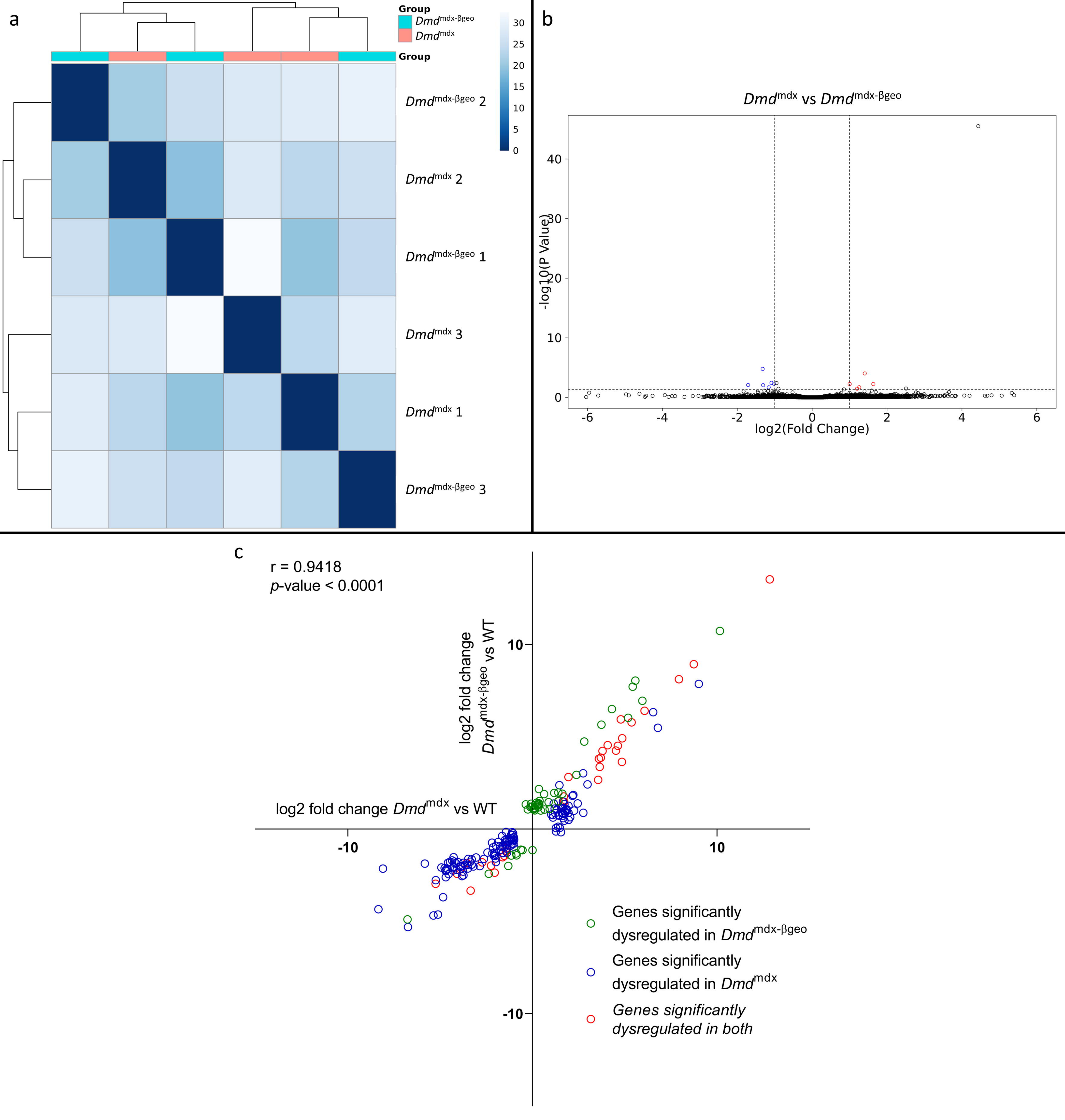
a
Group
$Dmd^{mdx\text{-}\beta geo}$
Dmd^{mdx}
Group
30
25
20
15
10
5
0
$Dmd^{mdx\text{-}\beta geo}$ 2
Dmd^{mdx} 2
$Dmd^{mdx\text{-}\beta geo}$ 1
Dmd^{mdx} 3
Dmd^{mdx} 1
$Dmd^{mdx\text{-}\beta geo}$ 3
b
Dmd^{mdx} vs $Dmd^{mdx\text{-}\beta geo}$
-log10(P Value)
40
30
20
10
0
-6
-4
-2
0
2
4
6
log2(Fold Change)
c
r = 0.9418
p-value < 0.0001
log2 fold change $Dmd^{mdx\text{-}\beta geo}$ vs WT
log2 fold change Dmd^{mdx} vs WT
10
-10
10
-10
Genes significantly dysregulated in $Dmd^{mdx\text{-}\beta geo}$
Genes significantly dysregulated in Dmd^{mdx}
Genes significantly dysregulated in both

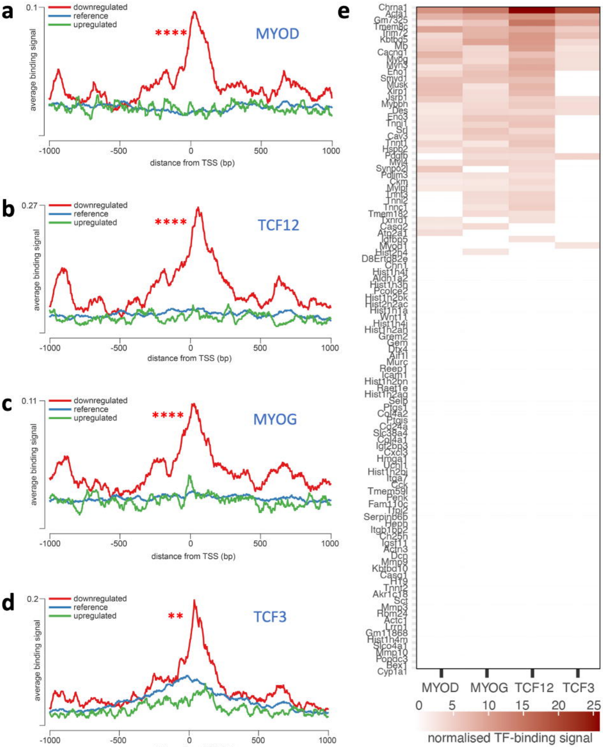
a
0.1
downregulated
reference
upregulated
****
MYOD
average binding signal
-1000
-500
0
500
1000
distance from TSS (bp)
b
0.27
downregulated
reference
upregulated
****
TCF12
average binding signal
-1000
-500
0
500
1000
distance from TSS (bp)
c
0.11
downregulated
reference
upregulated
****
MYOG
average binding signal
-1000
-500
0
500
1000
distance from TSS (bp)
d
0.2
downregulated
reference
upregulated
**
TCF3
average binding signal
-1000
-500
0
500
1000
distance from TSS (bp)
e
Chrna1
Acta1
Gm7325
Tmem8c
Trim72
Kbtbd5
Mb
Cacng1
Myog
Myh3
Eno1
Smyd1
Musk
Xirp1
Jsrp1
Mybph
Des
Eno3
Tnni1
Srl
Cav3
Tnnt1
Hspb2
Pdgfb
Myl4
Synpo2l
Pdlim3
Ckm
Mylpf
Tnnt3
Tnni2
Tnnc1
Tmem182
Txnrd1
Casq2
Atp2a1
Igfbp5
Myod1
Hist2h4
D8Ertd82e
Chn1
Hist1h4f
Aldh1a2
Hist1h3b
Pcolce2
Hist1h2bk
Hist2h2ac
Hist1h1a
Wnt11
Hist1h4j
Hist1h2ah
Grem2
Gem
Dtx4
Aif1l
Murc
Reep1
Icam1
Hist1h2bn
Raet1e
Hist1h2ag
Selp
Ptgs1
Col4a2
Ptgis
Cd24a
Slc38a4
Col4a1
Igf2bp3
Cxcl3
Hmga1
Uchl1
Hist1h2bj
Itga7
Cck
Tmem59l
Penk
Fam110c
Tfpi2
Serpinb6b
Heph
Itgb1bp2
Ch25h
Igsf11
Actn3
Dcn
Mmp9
Kbtbd10
Casq1
H19
Tnnt2
Akr1c18
Sct
Mmp3
Rbm24
Actc1
Lrrn1
Gm11868
Hist1h4m
Slco4a1
Mmp10
Popdc3
Bex1
Cyp1a1
MYOD
MYOG
TCF12
TCF3
0
5
10
15
20
25
normalised TF-binding signal

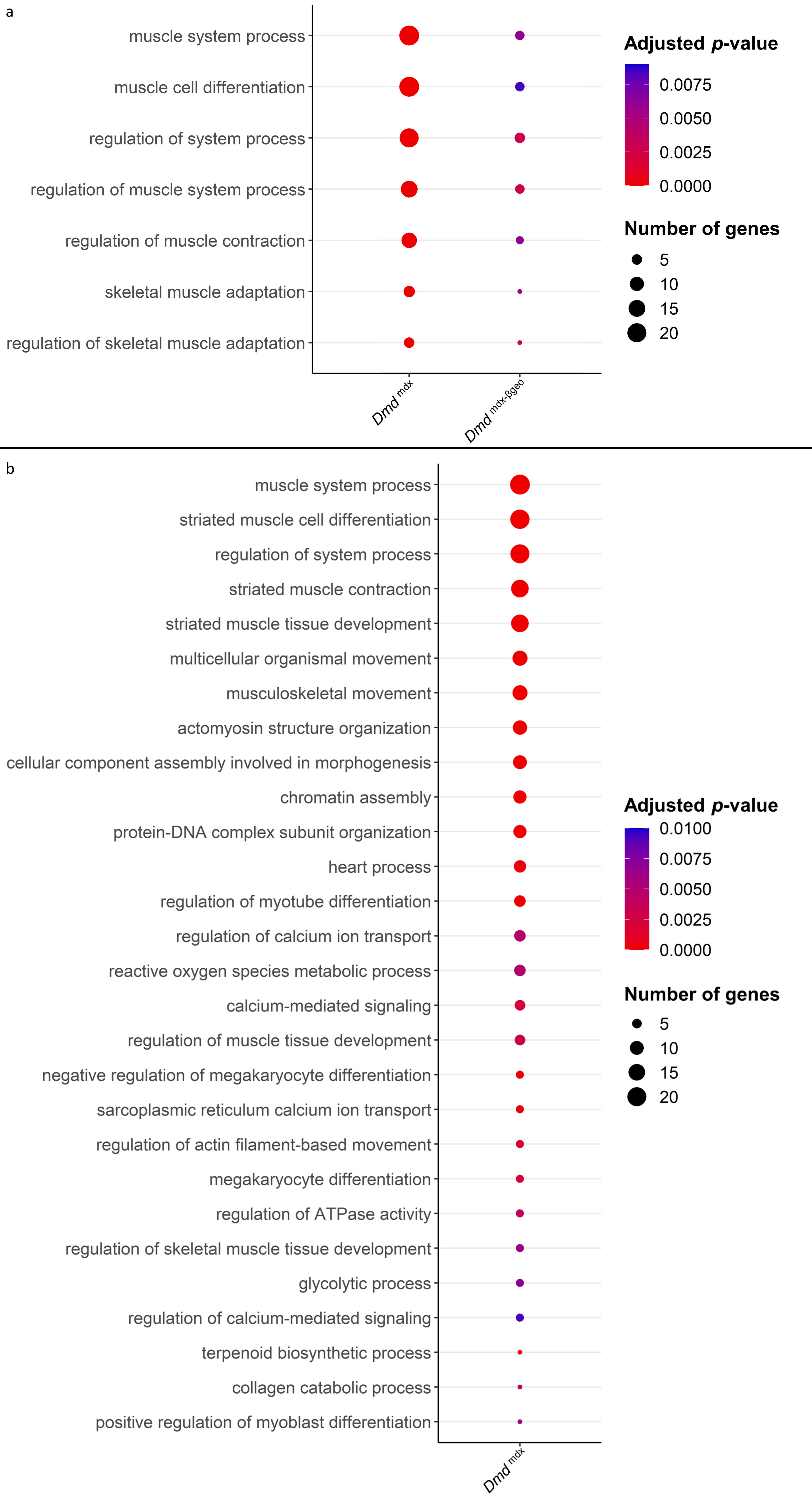
a
muscle system process
muscle cell differentiation
regulation of system process
regulation of muscle system process
regulation of muscle contraction
skeletal muscle adaptation
regulation of skeletal muscle adaptation
Dmd mdx
Dmd mdx-βgeo
Adjusted p-value
0.0075
0.0050
0.0025
0.0000
Number of genes
5
10
15
20
b
muscle system process
striated muscle cell differentiation
regulation of system process
striated muscle contraction
striated muscle tissue development
multicellular organismal movement
musculoskeletal movement
actomyosin structure organization
cellular component assembly involved in morphogenesis
chromatin assembly
protein-DNA complex subunit organization
heart process
regulation of myotube differentiation
regulation of calcium ion transport
reactive oxygen species metabolic process
calcium-mediated signaling
regulation of muscle tissue development
negative regulation of megakaryocyte differentiation
sarcoplasmic reticulum calcium ion transport
regulation of actin filament-based movement
megakaryocyte differentiation
regulation of ATPase activity
regulation of skeletal muscle tissue development
glycolytic process
regulation of calcium-mediated signaling
terpenoid biosynthetic process
collagen catabolic process
positive regulation of myoblast differentiation
Dmd mdx
Adjusted p-value
0.0100
0.0075
0.0050
0.0025
0.0000
Number of genes
5
10
15
20

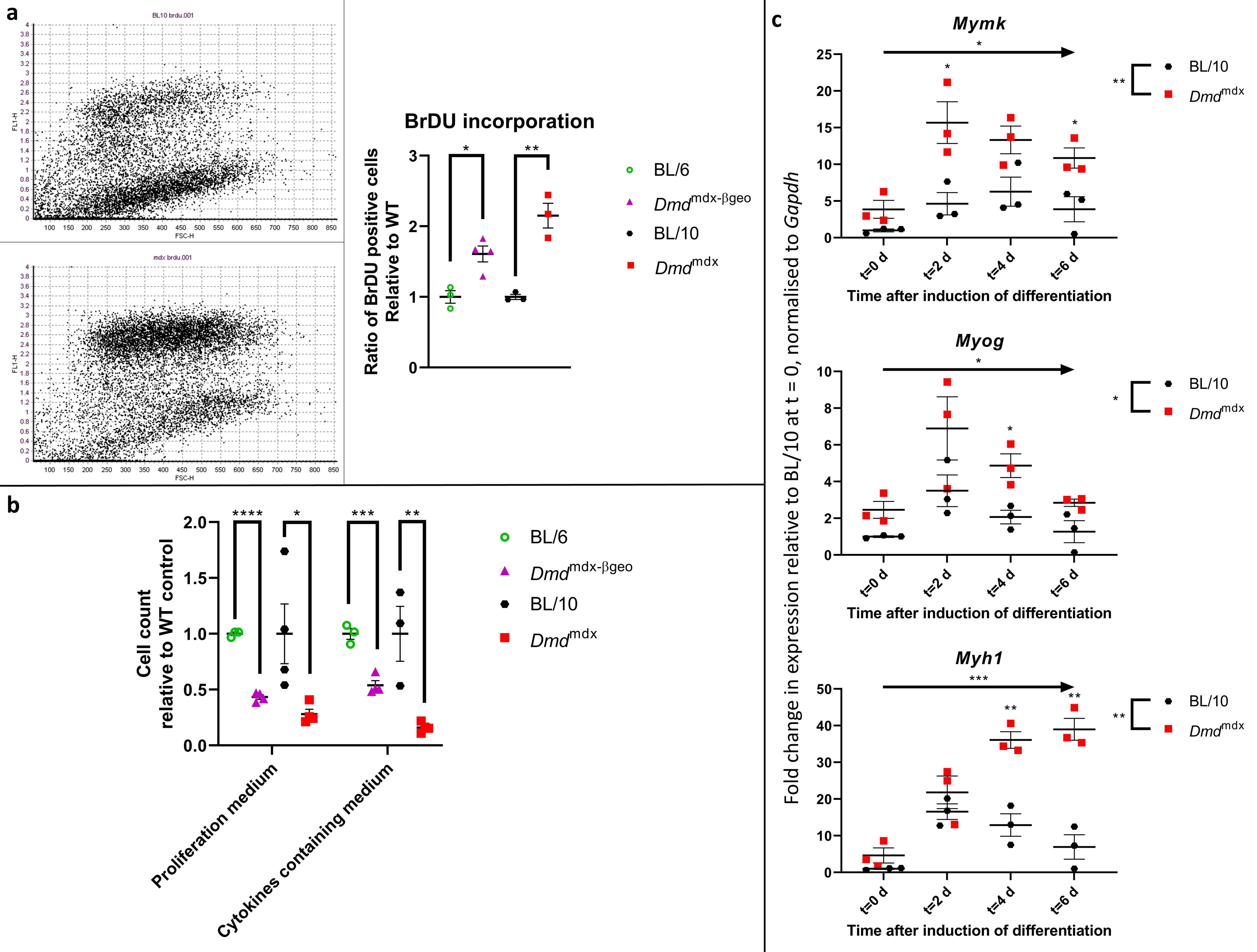
a
BL10 brdu.001
FL1-H
FSC-H
mdx brdu.001
FL1-H
FSC-H
BrDU incorporation
Ratio of BrDU positive cells Relative to WT
*
**
BL/6
Dmd^mdx-βgeo
BL/10
Dmd^mdx
b
Cell count relative to WT control
****
*
***
**
Proliferation medium
Cytokines containing medium
BL/6
Dmd^mdx-βgeo
BL/10
Dmd^mdx
c
Mymk
Myog
Myh1
Fold change in expression relative to BL/10 at t = 0, normalised to Gapdh
t=0 d
t=2 d
t=4 d
t=6 d
Time after induction of differentiation
BL/10
Dmd^mdx
*
**
***

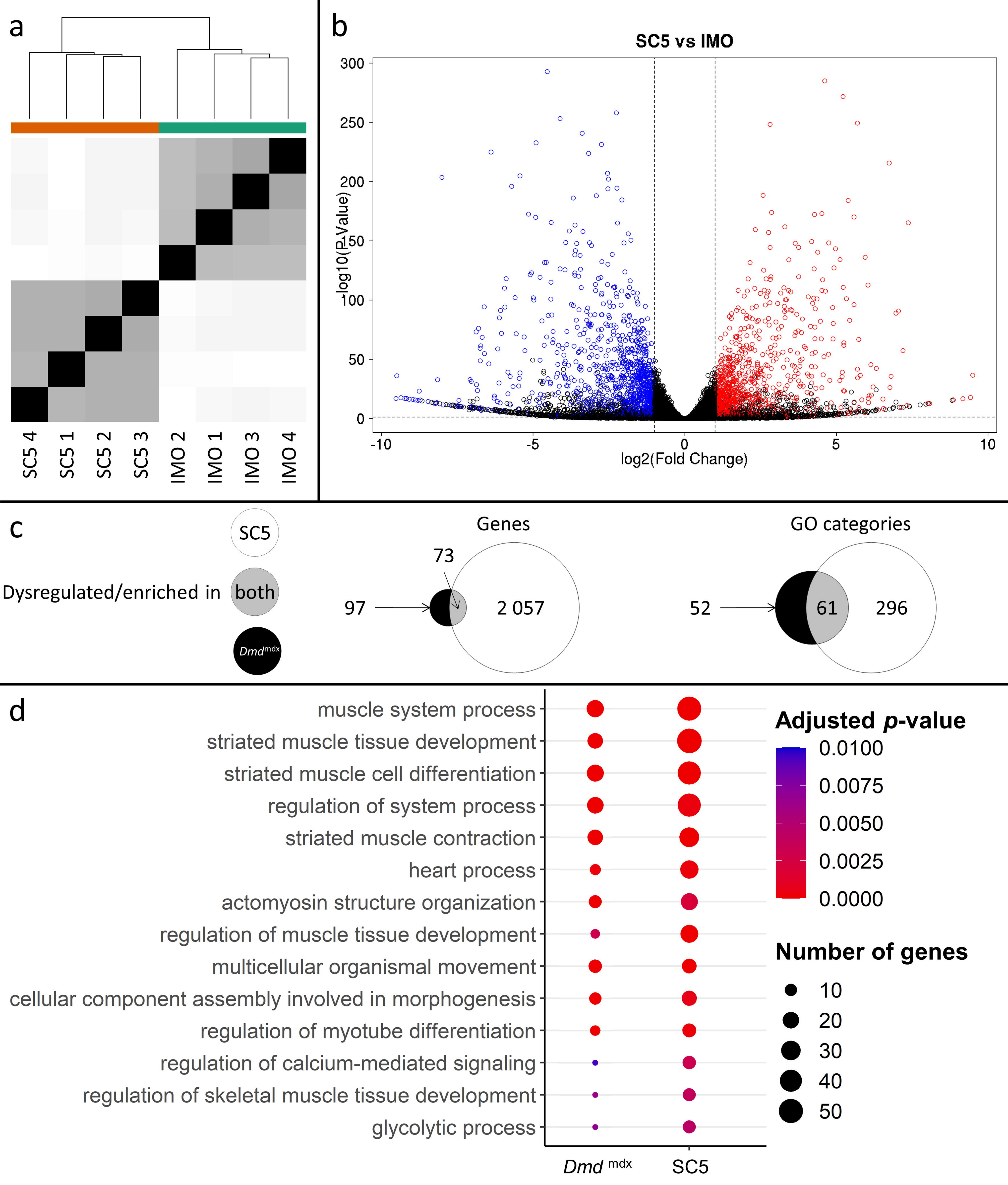
a
SC5 4
SC5 1
SC5 2
SC5 3
IMO 2
IMO 1
IMO 3
IMO 4
b
SC5 vs IMO
-log10(P-Value)
300
250
200
150
100
50
0
-10
-5
0
5
10
log2(Fold Change)
c
SC5
Dysregulated/enriched in
both
Dmd mdx
Genes
97
73
2 057
GO categories
52
61
296
d
muscle system process
striated muscle tissue development
striated muscle cell differentiation
regulation of system process
striated muscle contraction
heart process
actomyosin structure organization
regulation of muscle tissue development
multicellular organismal movement
cellular component assembly involved in morphogenesis
regulation of myotube differentiation
regulation of calcium-mediated signaling
regulation of skeletal muscle tissue development
glycolytic process
Dmd mdx
SC5
Adjusted p-value
0.0100
0.0075
0.0050
0.0025
0.0000
Number of genes
10
20
30
40
50

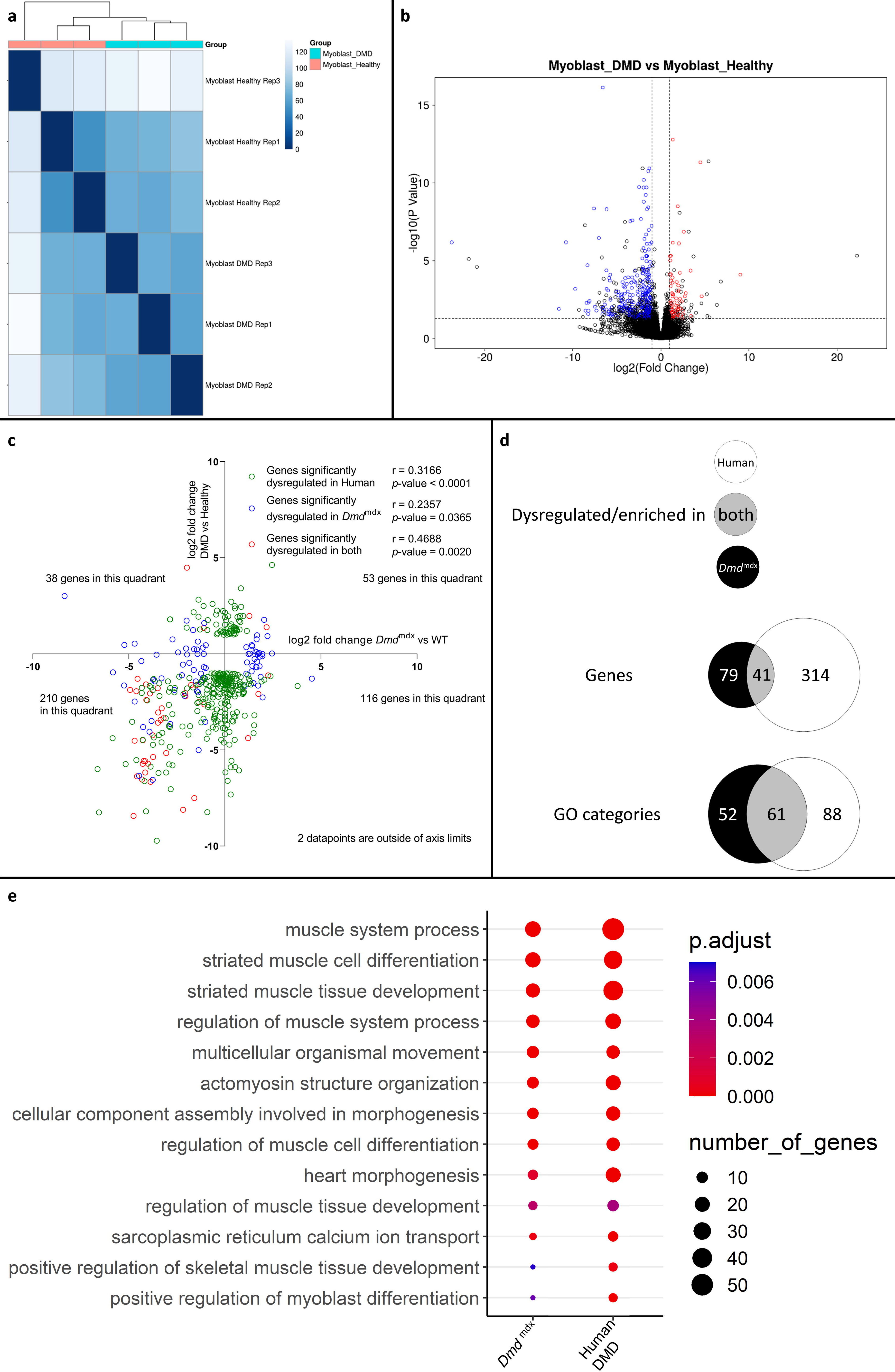
a
Group
120
100
80
60
40
20
0
Group
Myoblast_DMD
Myoblast_Healthy
Myoblast Healthy Rep3
Myoblast Healthy Rep1
Myoblast Healthy Rep2
Myoblast DMD Rep3
Myoblast DMD Rep1
Myoblast DMD Rep2
b
Myoblast_DMD vs Myoblast_Healthy
-log10(P Value)
15
10
5
0
-20
-10
0
10
20
log2(Fold Change)
c
log2 fold change DMD vs Healthy
10
5
-5
-10
Genes significantly dysregulated in Human
r = 0.3166
p-value < 0.0001
Genes significantly dysregulated in Dmd^mdx
r = 0.2357
p-value = 0.0365
Genes significantly dysregulated in both
r = 0.4688
p-value = 0.0020
38 genes in this quadrant
53 genes in this quadrant
log2 fold change Dmd^mdx vs WT
-10
-5
5
10
210 genes in this quadrant
116 genes in this quadrant
2 datapoints are outside of axis limits
d
Human
Dysregulated/enriched in
both
Dmd^mdx
Genes
79
41
314
GO categories
52
61
88
e
muscle system process
striated muscle cell differentiation
striated muscle tissue development
regulation of muscle system process
multicellular organismal movement
actomyosin structure organization
cellular component assembly involved in morphogenesis
regulation of muscle cell differentiation
heart morphogenesis
regulation of muscle tissue development
sarcoplasmic reticulum calcium ion transport
positive regulation of skeletal muscle tissue development
positive regulation of myoblast differentiation
Dmd mdx
Human DMD
p.adjust
0.006
0.004
0.002
0.000
number_of_genes
10
20
30
40
50

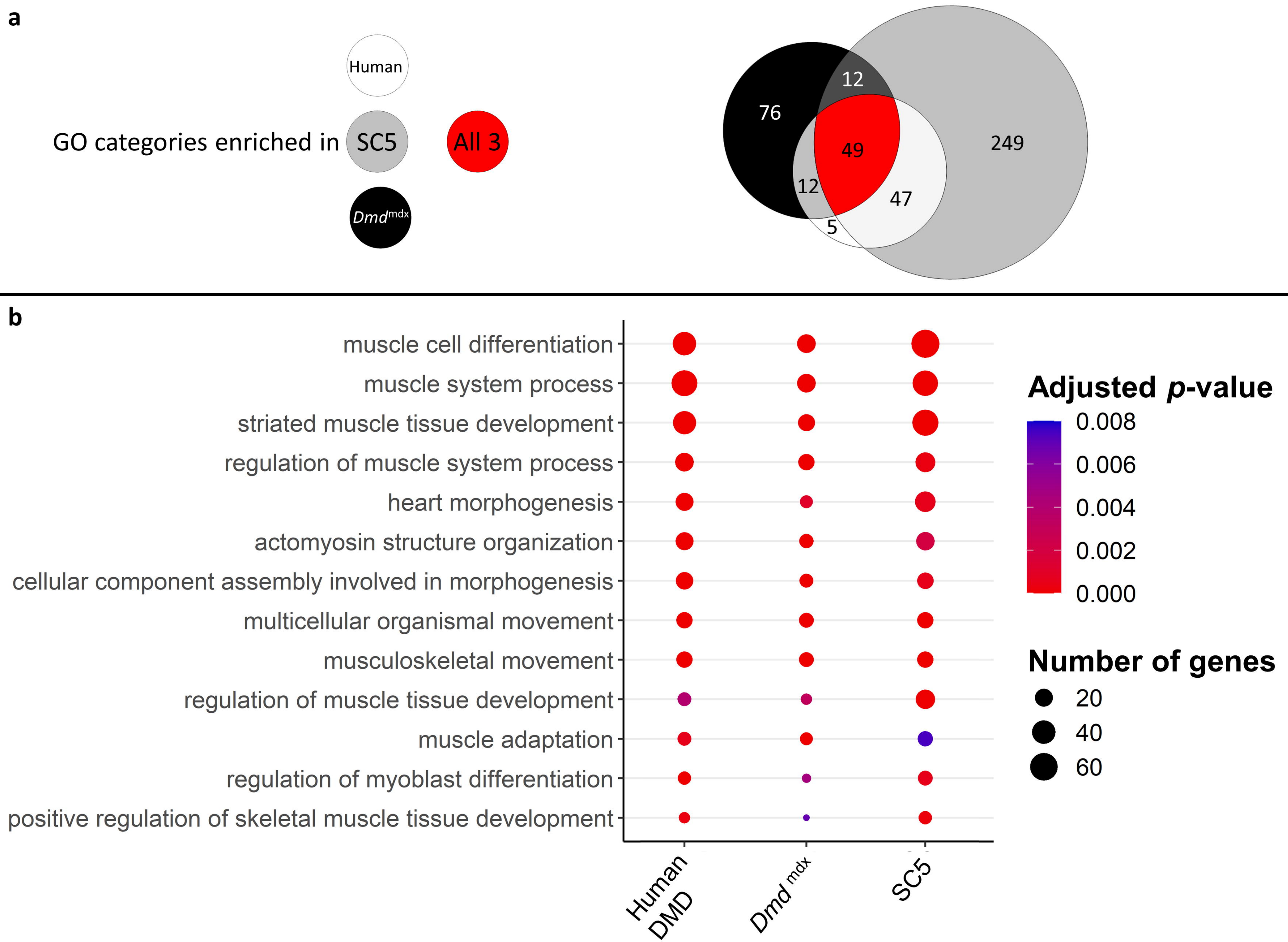
a
Human
GO categories enriched in
SC5
All 3
Dmd mdx
76
12
49
249
12
47
5
b
muscle cell differentiation
muscle system process
striated muscle tissue development
regulation of muscle system process
heart morphogenesis
actomyosin structure organization
cellular component assembly involved in morphogenesis
multicellular organismal movement
musculoskeletal movement
regulation of muscle tissue development
muscle adaptation
regulation of myoblast differentiation
positive regulation of skeletal muscle tissue development
Human DMD
Dmd mdx
SC5
Adjusted p-value
0.008
0.006
0.004
0.002
0.000
Number of genes
20
40
60

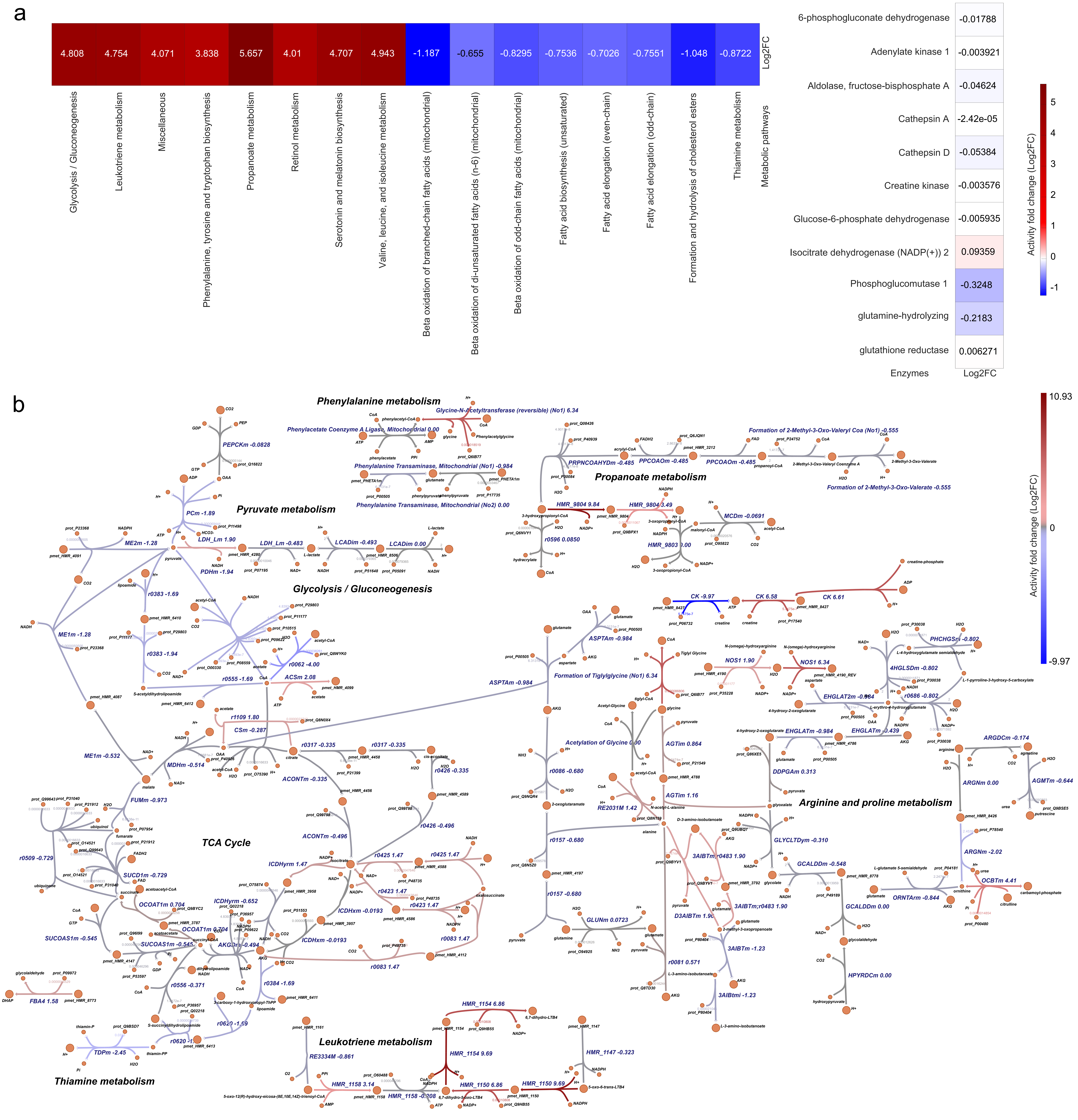
a
4.808
4.754
4.071
3.838
5.657
4.01
4.707
4.943
-1.187
-0.655
-0.8295
-0.7536
-0.7026
-0.7551
-1.048
-0.8722
Log2FC
Glycolysis / Gluconeogenesis
Leukotriene metabolism
Miscellaneous
Phenylalanine, tyrosine and tryptophan biosynthesis
Propanoate metabolism
Retinol metabolism
Serotonin and melatonin biosynthesis
Valine, leucine, and isoleucine metabolism
Beta oxidation of branched-chain fatty acids (mitochondrial)
Beta oxidation of di-unsaturated fatty acids (n-6) (mitochondrial)
Beta oxidation of odd-chain fatty acids (mitochondrial)
Fatty acid biosynthesis (unsaturated)
Fatty acid elongation (even-chain)
Fatty acid elongation (odd-chain)
Formation and hydrolysis of cholesterol esters
Thiamine metabolism
Metabolic pathways
6-phosphogluconate dehydrogenase -0.01788
Adenylate kinase 1 -0.003921
Aldolase, fructose-bisphosphate A -0.04624
Cathepsin A -2.42e-05
Cathepsin D -0.05384
Creatine kinase -0.003576
Glucose-6-phosphate dehydrogenase -0.005935
Isocitrate dehydrogenase (NADP(+)) 2 0.09359
Phosphoglucomutase 1 -0.3248
glutamine-hydrolyzing -0.2183
glutathione reductase 0.006271
Enzymes
Log2FC
Activity fold change (Log2FC)
5
4
3
2
1
0
-1
b
Phenylalanine metabolism
Glycine-N-Acetyltransferase (reversible) (No1) 6.34
Phenylacetate Coenzyme A Ligase, Mitochondrial 0.00
Phenylalanine Transaminase, Mitochondrial (No1) -0.984
Phenylalanine Transaminase, Mitochondrial (No2) 0.00
Pyruvate metabolism
PEPCKm -0.0828
PCm -1.89
LDH_Lm 1.90
LDH_Lm -0.483
LCADim -0.493
LCADim 0.00
ME2m -1.28
PDHm -1.94
Glycolysis / Gluconeogenesis
r0383 -1.69
r0383 -1.94
r0062 -4.00
ACSm 2.08
r0555 -1.69
ME1m -1.28
r1109 1.80
CSm -0.287
r0317 -0.335
r0317 -0.335
ME1m -0.532
MDHm -0.514
ACONTm -0.335
r0426 -0.335
FUMm -0.973
r0426 -0.496
ACONTm -0.496
TCA Cycle
r0509 -0.729
SUCD1m -0.729
ICDHyrm 1.47
r0425 1.47
r0425 1.47
r0423 1.47
r0423 1.47
OCOAT1m 0.704
OCOAT1m 0.704
ICDHyrm -0.652
ICDHxm -0.0193
ICDHxm -0.0193
SUCOAS1m -0.545
SUCOAS1m -0.545
AKGDm -0.494
r0083 1.47
r0083 1.47
r0384 -1.69
r0556 -0.371
FBA4 1.58
r0620 -1.69
r0620 -1.69
TDPm -2.45
Thiamine metabolism
Leukotriene metabolism
HMR_1154 6.86
HMR_1154 9.69
RE3334M -0.861
HMR_1158 3.14
HMR_1158 -0.208
HMR_1150 6.86
HMR_1150 9.69
HMR_1147 -0.323
Propanoate metabolism
PRPNCOAHYDm -0.485
PPCOAOm -0.485
PPCOAOm -0.485
Formation of 2-Methyl-3-Oxo-Valeryl Coa (No1) -0.555
Formation of 2-Methyl-3-Oxo-Valerate -0.555
HMR_9804 9.84
HMR_9804 3.49
MCDm -0.0691
r0596 0.0850
HMR_9803 0.00
CK -9.97
CK 6.58
CK 6.61
ASPTAm -0.984
ASPTAm -0.984
Formation of Tiglylglycine (No1) 6.34
NOS1 1.90
NOS1 6.34
PHCHGSm -0.802
4HGLSDm -0.802
EHGLAT2m -0.984
r0686 -0.802
EHGLATm -0.984
EHGLATm -0.439
ARGDCm -0.174
Acetylation of Glycine 0.00
AGTim 0.864
AGTim 1.16
DDPGAm 0.313
r0086 -0.680
RE2031M 1.42
AGMTm -0.644
ARGNm 0.00
Arginine and proline metabolism
r0157 -0.680
r0157 -0.680
3AIBTm;r0483 1.90
GLYCLTDym -0.310
ARGNm -2.02
GCALDDm -0.548
OCBTm 4.41
D3AIBTm 1.90
3AIBTm;r0483 1.90
ORNTArm -0.844
GCALDDm 0.00
GLUNm 0.0723
3AIBTm -1.23
r0081 0.571
3AIBtmi -1.23
HPYRDCm 0.00
Activity fold change (Log2FC)
10.93
0
-9.97

Developing muscle

Adult muscle

Norm:

Expression of:
Dp71
Dp412e (human)
Dp427
Dp427m, complete DAPC

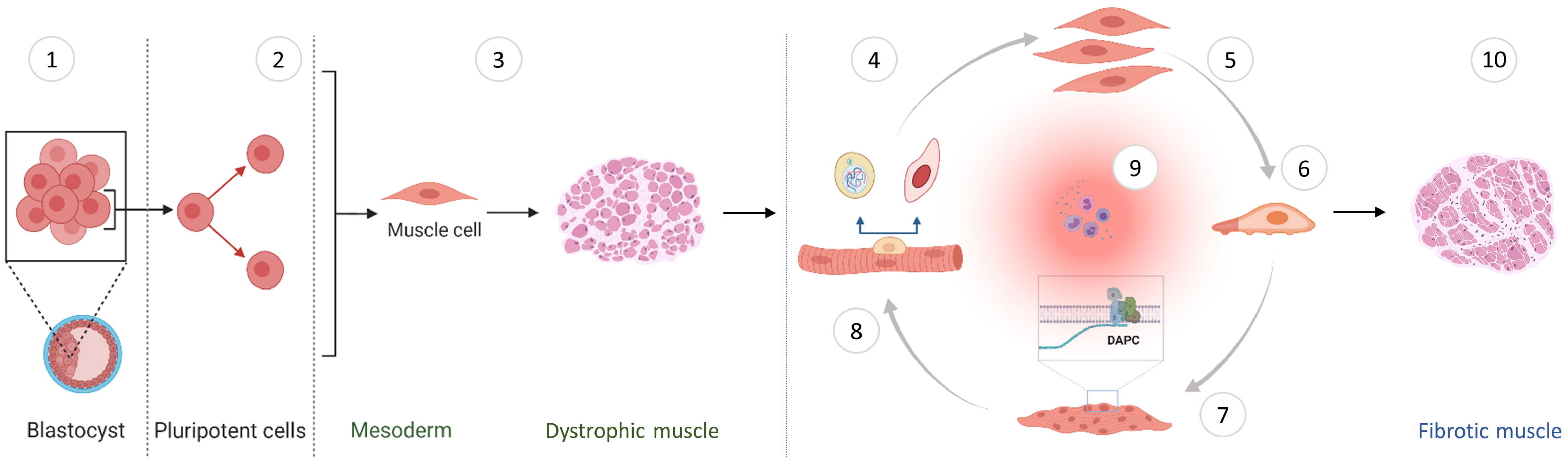
1
2
3
4
5
6
7
8
9
10
Muscle cell
DAPC
Blastocyst
Pluripotent cells
Mesoderm
Dystrophic muscle
Fibrotic muscle

DMD manifests before cell entry into skeletal muscle compartment.

Disrupted myogenesis: Myotube formation and stem cell defects.

Embryonic DMD muscle damaged.

DMD manifests in SC, proliferating myoblasts, differentiating myotubes and in myofibres. Inflammation contributes to both muscle damage and regeneration.

Connective tissue replaces muscle

Created with BioRender.com